

**COMPUTATIONAL STUDY AND ERROR ANALYSIS OF AN INTEGRATED
SAMPLING-PROBE AND GAS-ANALYZER FOR MIXING MEASUREMENTS
IN SUPERSONIC FLOWS**

by

Wenbo Zhu

THESIS

Submitted in partial fulfillment of the requirements for the degree of Master of Science in
Aerospace Engineering at The University of Texas at Arlington

May, 2016

Arlington, Texas

Supervising Committee:

Dr. Luca Maddalena, Supervising Professor

Dr. Frank Lu

Dr. Donald Wilson

Abstract

Computational Study and Error Analysis of an Integrated Sampling-Probe and Gas-Analyzer for Mixing Measurements in Supersonic Flows

Wenbo Zhu, M.S.

The University of Texas at Arlington, 2016

Supervising Professor: Luca Maddalena

Concentration probes are employed in supersonic flow mixing experiments for binary gas mixture composition measurements. These measurements are fundamental for the advancement of the scramjet technology. While non-intrusive laser-based methods (such as planar laser-induced fluorescence and filtered Rayleigh scattering) have been developed greatly over the past few decades, intrusive methods (such as concentration probes) still play an essential role in the measurement of mixture composition due to the fact that, with correct application, they do not require further assumptions on the aerothermodynamic states of the investigated mixture, which are often difficult to corroborate. Conversely, such assumptions are essential to the measurement of the mixture composition with current non-intrusive methods. Because the typical design of these probes is essentially based on an inviscid, adiabatic, quasi-one-dimensional analysis, the scope of this work is to better

understand and quantify the severe impact of viscous effects on the probe's internal gasdynamics and the associated uncertainties in the measured quantities via a computational fluid dynamics analysis. Specifically, the focus is on the augmented errors due to the aforementioned viscous effects when coupled with various cases of probe-flow misalignment, which is a typical scenario encountered in mixing measurements of binary gas compositions (air and helium mixture in the present work) in vortex-dominated flows. Results, new in literature, show phenomena such as shock-induced boundary layer separation and the formation of an oblique shock train. These flow features are found to noticeably affect the accuracy of the composition measurement. The errors associated with the inviscid, adiabatic, quasi-one-dimensional analysis of the probes are quantified in this study. The computational model developed in this work is also used to design a probe that can minimize such errors in mixture composition measurements.

Copyright by

Wenbo Zhu

2016

Acknowledgements

I would like to first thank my family for their support before and during my study in the United States. They always tell me to trust myself and pursue what I truly like. I cannot ever repay them in enough ways for raising me and supporting me.

I would also like to express a deep gratitude to my research advisor Dr. Luca Maddalena. After coming to the University of Texas at Arlington (UTA) and finishing the undergraduate courses I was required to make up, Dr. Maddalena was willing to give me an opportunity to work on a very interesting project on aerodynamics. Through constant feedback and high expectations, he has helped me to grow as an engineer and gain more understanding of this field. I look up to him as my mentor and I appreciate the patience and help he has given to me during my pursuit of the master's degree. I'd also like to thank my defense committee members Dr. Lu and Dr. Wilson for their time and effort in reviewing my thesis.

Additionally, I would like to thank the group members in Dr. Maddalena's team and the Aerodynamics Research Center community, especially Dr. Fabrizio Vegine, Dr. Stefano Gulli, doctoral student Cody Ground and laboratory manager David Carter for their assistance in the past two years.

Finally, I would like to thank the Mechanical and Aerospace Engineering Department at UTA for giving me the chance to pursue a degree in Aerospace Engineering.

May 04, 2016

Table of Contents

Abstract.....	ii
Acknowledgements.....	v
Table of Contents.....	vi
List of Figures.....	viii
List of Tables.....	xi
Chapter 1 Introduction.....	1
1.1 Background.....	1
1.2 Previous Concentration Probe Designs.....	2
1.3 Experimental Setup for the Current Probe.....	5
1.4 Contribution of the Current Study.....	6
Chapter 2 Working Principle of the Concentration Probe.....	8
2.1 Internal Gasdynamics.....	8
2.2 Principle of Operation.....	11
2.3 Probe Calibration.....	14
Chapter 3 Characteristics of the Current Probe.....	17
3.1 Details of the Probe Considered in Current Study.....	17
3.2 Characteristics of the Probe’s Internal Gasdynamics.....	19
3.3 Characteristics of the Probe’s External Gasdynamics.....	22
3.4 Frequency Response of the Current Probe.....	25
Chapter 4 Computational Models and Methods.....	30
4.1 Geometry Used in the Computational Domain.....	30
4.2 Meshing Strategy.....	32
4.3 Solver Setup.....	34
Chapter 5 Computational Results and Discussion.....	37
5.1 Grid Independence Study.....	37
5.2 Mean Flow Characteristics of an Adiabatic Probe.....	39
5.3 Error Analysis of Helium-Air Composition Measurements.....	47

Chapter 6 CFD-aided New Probe Design.....	54
6.1 Testbed Based on the CFD Study.....	54
6.2 Quasi-one-dimensional Characteristics of the Testbed.....	58
6.3 CFD Setup of the Tesbed.....	59
6.4 Computational Results on the Testbed Geometry.....	63
Chapter 7 Conclusion.....	74
7.1 Summary of the CFD Findings and Recommendations.....	74
7.2 Future Work.....	75
References.....	77
Biographical Information.....	79
Appendix A Matlab Scripts.....	80
A.1 Inviscid, Quasi-one-dimensional Analysis Code.....	81
A.2 Probe Calibration Code.....	91

List of Figures

Figure 1.1: Geometry of the probe made by Brown and Rebollo.....	2
Figure 1.2: Geometry of the concentration probe designed by Ninnemann and Ng.....	4
Figure 1.3: Geometry of the concentration probe made by Wiswall.....	5
Figure 1.4: Fuel injector in the supersonic wind tunnel at ARC.....	6
Figure 2.1: Schematic of the probe's generic gasdynamics.....	9
Figure 2.2: Schematic of the hot-film in the sensing plane with uniform flow assumption.....	12
Figure 2.3: Calibration setup (a) the overall setup (b) a close look on the probe.....	15
Figure 2.4: Example of calibration curves from a calibration operation.....	16
Figure 3.1: 2D schematic of the two-throat probe used in this work.....	18
Figure 3.2: Mach number and cross-sectional area along the internal length of the studied probe for $M_\infty = 2.2$	20
Figure 3.3: Ratio of static temperature over total temperature along the probe axial length for $M_\infty = 2.2$	21
Figure 3.4: Ratio of static pressure over total pressure along the probe for $M_\infty = 2.2$	21
Figure 3.5: Three-dimensional plot of the maximum allowable flow angularities for freestream conditions at 10h.....	24
Figure 3.6: Flow at the probe tip of ideal and real cases.....	25
Figure 4.1: A transparent isometric view of the probe.....	31
Figure 4.2: Meshing strategy (a) the overall computational domain with two bodies of	

influence highlighted (b) mesh at the XY plane (c) zoomed view around the probe tip.....	33
Figure 4.3: Boundary conditions setup shown with a XY-plane cut of the computational domain.....	35
Figure 5.1: Mach number contour (a) in the XY plane (b) zoomed view around the first diverging section.....	38
Figure 5.2: Comparison of Mach number along the axial center of the probe.....	39
Figure 5.3: Flow visualization by the numerical Schlieren.....	40
Figure 5.4: Streamlines (a) at the first diverging section in the XY plane (b) at the second diverging section in the XY plane (c) at the second diverging section in the XZ plane.....	42
Figure 5.5: Mach number contours in the first diverging section in the XY plane as an effect of the flow angularity (a) pure air, 5° AoA (b) pure air, 10° AoA (c) pure helium, 5° AoA (d) pure helium, 10° AoA.....	46
Figure 5.6: Schematic of flows at the sensing plane (a) with uniform flow assumption (b) without uniform flow assumption.....	48
Figure 5.7: Illustration of the error in the helium concentration measurement.....	49
Figure 5.8: Mass flow rate measurement (a) “hot-film” element (b) meshing around the “hot-film” (c) velocity profile along the sensing plane in the pure air 0° AoA case.....	50
Figure 6.1: Dimension of the modified probe cap in English units.....	56
Figure 6.2: Mesh of the testbed probe (a) with 14 local refinements to study the proper hot-film location (b) mesh around the sensing elements.....	57
Figure 6.3: Mach number and cross-sectional area along the axial length inside the	

tesbed.....	59
Figure 6.4: Schematic of the flow in probe calibrations.....	60
Figure 6.5: Pt2/Pt1 of the original two-throat probe calibration (a) data of 11 helium concentrations (b) data of the pure air case.....	61
Figure 6.6: Part of the computational domain for the simulated calibration case.....	62
Figure 6.7: Boundary and initial conditions of the testbed in the simulated calibration.....	63
Figure 6.8: Mach number contour around the tip of the tesbed in the simulated SSWT test, pure air case.....	64
Figure 6.9: Streamlines of the testbed in the simulated SSWT test, pure air case (a) frontal part of the probe (b) aft part of the probe.....	65
Figure 6.10: Mach number contour of the testbed in the simulated calibration, pure air case.....	66
Figure 6.11: Streamlines of the testbed in the simulated calibration, pure air case (a) frontal part of the probe (b) aft part of the probe.....	67
Figure 6.12: Comparison of velocity profiles along the probe's internal diameter at sampling locations between the simulated SSWT and the simulated calibration for pure air case.....	69
Figure 6.12 (cont.): Comparison of velocity profiles along the probe's internal diameter at sampling locations between the simulated SSWT and the simulated calibration for pure air case.....	70

List of Tables

Table 3.1: Characteristics of the current probe based on the inviscid quasi-one-dimensional analysis.....	22
Table 3.2: Allowable flow angularity for attached shock under freestream conditions.....	23
Table 3.3: Summary of characteristics of the sensors used in the probe.....	27
Table 3.4: Fill time and flush time of the probe operating at 20°C.....	29
Table 4.1: Summary of the solver settings.....	36
Table 5.1: Mesh information of the grid independence study.....	38
Table 5.2: Predictions of the shock-induced boundary layer separation.....	44
Table 5.3: Error in helium concentration measurements.....	52
Table 6.1: Characteristics of the testbed design.....	58
Table 6.2: F factor at selected stations between the simulated SSWT test and calibration, pure air case.....	71
Table 6.3: F factor at selected stations between the simulated SSWT test and calibration, pure helium case.....	72

Chapter 1

Introduction

1.1 Background

It has been several decades since the start of research on air-breathing hypersonic vehicles. Over the years, many efforts have been made to make the combustion process in scramjet engines more efficient. One of the challenges in improving the combustion process in scramjet engines is to achieve effective mixing of the injected fuel and ingested air within the limited flow residence time in the combustor, which is on the order of milliseconds. Within this short residence time, the fuel and air need to be sufficiently mixed at the molecular level and react in order to produce the needed propulsion efficiency. Since the reaction of the fuel and air is a faster process compared to the flow residence time in the combustor, the overall process is said to be mixing limited.

Over the years, numerous experimental efforts have been made to improve the mixing efficiency of the fuel and air, but to characterize the effectiveness of any fuel and air mixing technique, the resulting mixture composition needs to be experimentally quantified. Several techniques for mixture composition measurements, of either an intrusive or non-intrusive nature, have been developed over the years. While non-intrusive laser-based methods (such as planar laser-induced fluorescence and filtered Rayleigh scattering) have been developed greatly over the past few decades, intrusive methods (such as concentration probes) still play an essential role in the measurement of mixture composition due to the

fact that, with correct application, they do not require further assumptions on the aerothermodynamic states of the investigated mixture, which are often difficult to corroborate. Conversely, such assumptions are essential to the measurement of the mixture composition with current non-intrusive methods.

1.2 Previous Concentration Probe Designs

It was Blackshear and Fingerson [1] who first adopted a probe geometry of a single hot-film sensor behind a choked orifice and recognized its ability to measure the composition of a binary mixture in subsonic flows. Later, Brown and Rebollo [2] used a similar design to measure the mean composition of a binary gas mixture at a constant temperature and pressure environment, which only works in a uniform subsonic flowfield. The probe is small but has a fast response and works very well in identifying the local composition, detecting 1% molar fraction of helium in air according to the authors. The geometry of this probe is shown in figure 1.1.

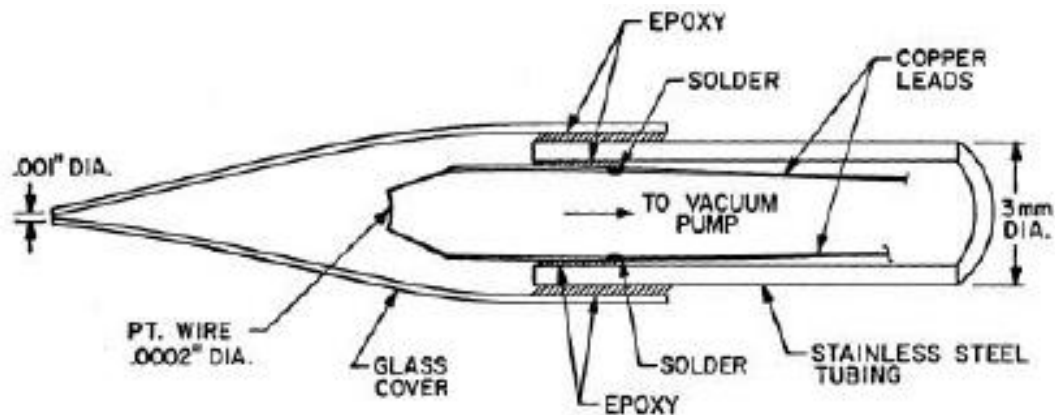


Figure 1.1 Geometry of the probe made by Brown and Rebollo [2].

While Brown and Rebollo's probe can only measure the mean composition of a binary gas mixture in subsonic flowfields, Devillers and Diep [3] later used a bare hot-wire probe to measure the mean composition in a supersonic flow. But in order to work, knowledge of the pressures and heat transfer conditions around the hot-wire is needed beforehand.

In 1992, Ninnemann and Ng [4] first built a concentration probe suitable for supersonic flow mixing measurements that has become the benchmark of such applications. Their probe consists of a small tip, a diverging section, a constant area section and a throat section, shown in figure 1.2. A vacuum pump is connected to the aft body of the probe to provide a low back pressure that ensures choked condition at the throat and a normal shock forming in the diverging section for isokinetic sampling during the operation. The details of the gasdynamics inside the probe will be discussed in chapter 2. A hot-film sensor and pressure tap are located inside the constant area section where the flow velocity is sufficiently low so that static conditions can be treated as total conditions. For mean composition measurements, the probe is found to produce less than 2.5% error in molar concentration measurements in helium-air gas mixtures with freestream flow angularity within 15° , and less than 2% error in molar concentration measurements when a 12°K variation in stagnation temperature exists. However, to measure the mixture mean composition, additional total temperature measurements of the flow at the same sampling positions are needed since the probe cannot measure the temperature by itself. Overall, their probe has a frequency response of 10 Hz, restricted by the pressure measurement using hypodermic

tubing.

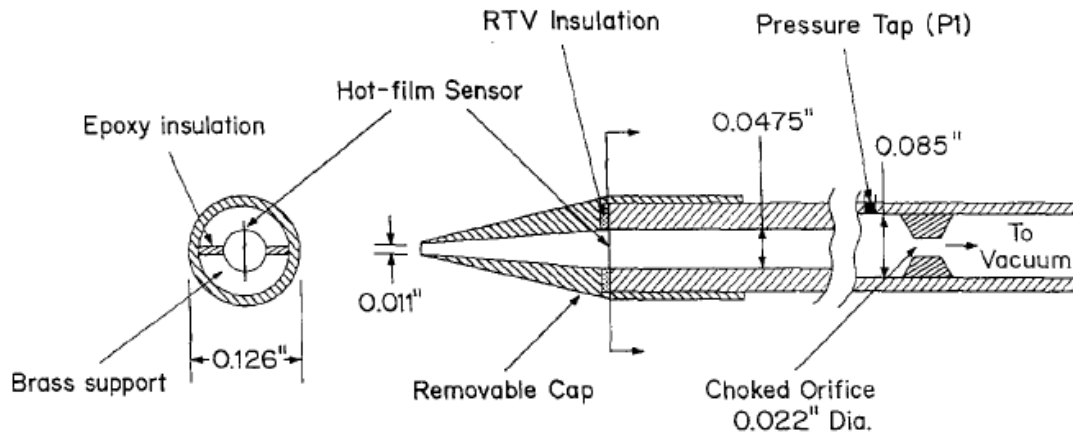


Figure 1.2 Geometry of the concentration probe designed by Ninnemann and Ng [4].

Several other concentration probes have been developed since then with various design modifications to improve the probe's performance and applicability range. In 2013, Wiswall [5] built a probe that adopted the advantages of several previous designs. The probe follows the general architecture from Ng's probe but uses two symmetrically placed throats and integrated miniaturized pressure transducer instead of using a pressure tap. Such modification can also be found in Xillo's probe [6]. In addition, it integrates a thermocouple for simultaneous total temperature measurements, which can also be found in Maddalena's probe [7]. The integration of three sensors (hot-film, miniaturized pressure transducer and thermocouple) in this probe improves the probe's frequency response, allowing larger portions of the flowfields to be probed during a typical run. The geometry is shown in figure 1.3 with highlight of the sensors integrated inside the probe.

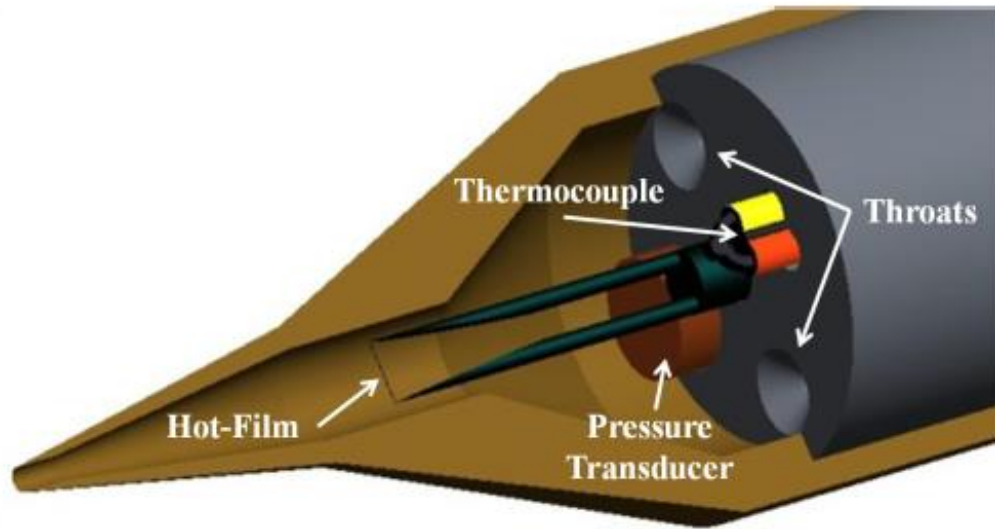


Figure 1.3 Geometry of the concentration probe made by Wiswall [5].

1.3 Experimental Setup for the Current Probe

The probe made by Wiswall and examined in this work is used in the supersonic wind tunnel (SSWT) of the Aerodynamics Research Center (ARC) at the University of Texas at Arlington (UTA) for composition measurements in a series of supersonic mixing studies. In these experiments, the blow-down type tunnel is set to provide Mach 2.5 cold flow entering the test section. Additionally, a strut injector is mounted in the wind tunnel's test section, simulating the hydrogen fuel injection in a counterpart non-reacting environment by injecting a passive scalar, helium. This strut injector also serves as a platform to enhance fuel and air mixing by introducing organized streamwise vorticity [8]. The concentration probe is placed downstream from the injector, and the downstream distance is normalized by the height of the ramp, h , installed on the injector. In this study, probe's sampling plane

conditions were taken from 10h downstream from the injector. With this setup, the probe can sample the resulting flowfield at the planar region to examine the mixing effectiveness of the introduced systems of streamwise vortices.

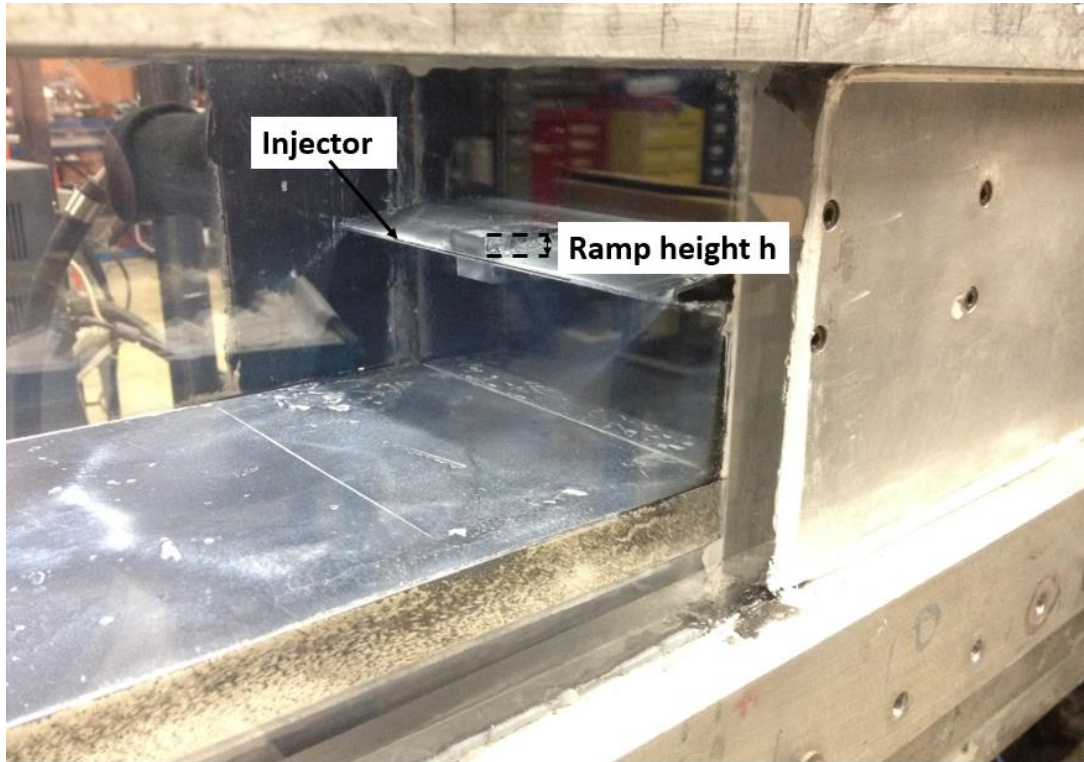


Figure 1.4 Fuel injector in the supersonic wind tunnel at ARC.

1.4 Contribution of the Current Study

Because the design of these probes is essentially based on an inviscid, adiabatic, quasi-one-dimensional analysis, the scope of this work is to better understand and quantify the severe impact of viscous effects on the probe's internal gasdynamics and the associated uncertainties in the measured quantities via a computational fluid dynamics analysis. Specifically, the focus is on the augmented errors due to the aforementioned viscous effects

when coupled with various cases of probe-flow misalignment, which is a typical scenario encountered in mixing measurements of binary gas compositions (air and helium mixture in the present work) in vortex-dominated flows. Results, new in literature, show phenomena such as shock-induced boundary layer separation and the formation of an oblique shock train. These flow features are found to noticeably affect the accuracy of the composition measurement. The errors associated with the inviscid, adiabatic, quasi-one-dimensional analysis of the probes are quantified in this study. The computational model developed in this work is also used to design a probe that can minimize such errors in mixture composition measurements.

Chapter 2

Working Principle of the Concentration Probe

The generic architecture of a concentration probe used in supersonic flow regime comes from Ninnemann and Ng [4]. A binary gas mixture mean composition is then determined by measuring the average mass flux over a hot-film sensor, and the total pressure and total temperature of the flow impinging on the hot-film. This chapter discusses in detail the working principles of this probe. The analysis used in this chapter is based on the classic adiabatic, inviscid, and quasi-one-dimensional flow assumption.

2.1 Internal Gasdynamics

The generic architecture of a concentration probe operating in supersonic flows is shown in figure 2.1, which highlights the flow regime (Mach number) in each key station along the probe. The probe consists of three main functioning sections: (1) an inlet, (2) a plenum chamber with constant cross-sectional area, and (3) a throat. In addition, a vacuum pump downstream is connected to the probe to provide a low back pressure so that the flow is always choked at the throat. The inlet is expanding so the flow expands supersonically until a normal shock is formed to allow the mass flow rate to pass through the probe's throat. The dimension of the inlet is chosen so that the normal shock is kept within the expanding inlet section and mixture liquefaction is avoided. The flow after the normal shock continues to decelerate and static conditions become more than 99.5% of the

stagnation conditions entering the probe's plenum chamber. Sensors are installed inside the plenum chamber where the cross-sectional area is kept constant. These sensors measure the variables (Constant Temperature Anemometer output voltage, total pressure and total temperature) that will be used to calculate the mixture composition. Finally, the flow accelerates towards the throat and becomes choked.

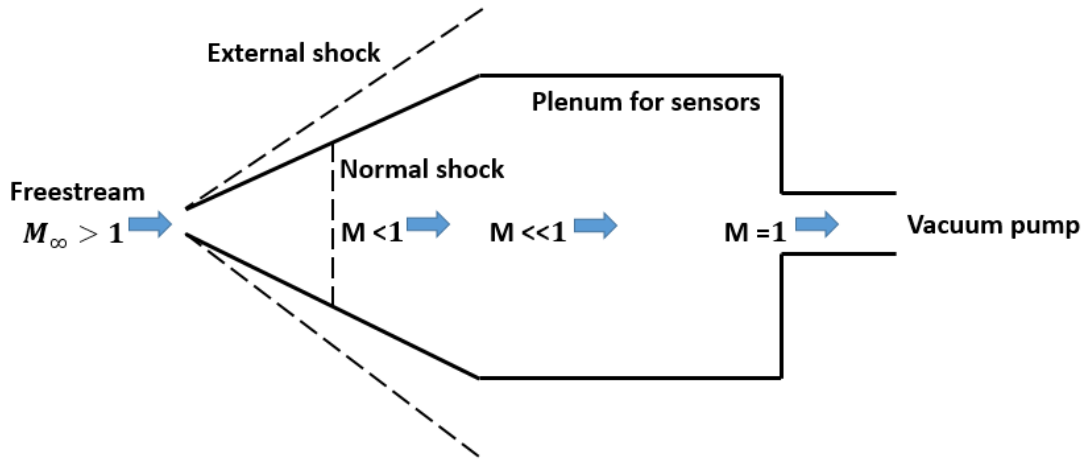


Figure 2.1 Schematic of the probe's generic gasdynamics.

The detailed flow conditions along the axial locations inside the probe can be found through an inviscid, adiabatic, quasi-one-dimensional analysis for a given freestream flow Mach number, gas composition and probe geometry. The area ratio between the inlet and the throat is a key design parameter and is chosen by the designer. This ratio will affect the flow conditions inside the probe by equation (2.1):

$$\frac{A_i}{A_t} = \frac{A_i A^*}{A^* A_t} = \frac{A_i P_{t,2}}{A^* P_{t,1}} \quad (2.1)$$

where A_i is the inlet cross-sectional area, A_t is the throat area, and A^* is the virtual throat area associated with the freestream Mach number M_∞ [9]. Because of the normal shock

inside the probe, A^*/A_t equals the ratio of the total pressure downstream and upstream of the shock $P_{t,2}/P_{t,1}$. To find the total pressure ratio, A^* needs to be known and it can be found through the isentropic relation (2.2) with the known M_∞ . At this point, the ratio between the total pressures is known and the Mach number upstream of the normal shock M_s can be found in (2.3):

$$\frac{A_t}{A^*} = \frac{1}{M_\infty} \left(\frac{2}{\gamma+1} \left(1 + \frac{\gamma-1}{2} M_\infty^2 \right) \right)^{\frac{\gamma+1}{2(\gamma-1)}} \quad (2.2)$$

$$\frac{P_{t,2}}{P_{t,1}} = \left[\frac{(\gamma+1)M_s^2}{(\gamma-1)M_s^2+2} \right]^{\frac{\gamma}{\gamma-1}} \left[\frac{\gamma+1}{2\gamma M_s^2 - (\gamma-1)} \right]^{\frac{1}{\gamma-1}} \quad (2.3)$$

where γ is the specific heat ratio of the binary gas mixture.

Therefore, with the knowledge of the Mach number upstream of the normal shock, the cross-sectional area of the shock plane A_s can be found through the isentropic relation shown in equation (2.4). Thus, the location of the normal shock inside the probe can be calculated from the geometry. This dimension is used to properly design the expanding inlet dimension so that the normal shock is trapped within the inlet and the expansion does not exceed the mixture's liquefaction temperature and pressure.

$$\frac{A_s}{A^*} = \frac{1}{M_s} \left[\frac{2}{\gamma+1} \left(1 + \frac{\gamma-1}{2} M_s^2 \right) \right]^{\frac{\gamma+1}{2(\gamma-1)}} \quad (2.4)$$

As both the flow upstream and downstream of the shock are isentropic, respectively, flow properties at any axial location inside the probe can now be found through the inviscid, adiabatic, quasi-one-dimensional analysis.

2.2 Principle of Operation

In the 1970's, Brown and Rebollo [2] conducted a dimensional analysis of a heated filament operating in a subsonic flow at constant temperature. For a hot-film used in conjunction with a Constant Temperature Anemometer (CTA) system, a dynamic balance is achieved between the Joule heating, proportional to the electrical current in the film imposed by the CTA, and the convective cooling due to the motion of the fluid mixture over the hot-film. Based on this principle, Brown and Rebollo developed a governing equation of composition measurement for a binary gas mixture. For an air-helium gas mixture, the helium concentration in mole fraction form, X_{He} , is found to be determined by the binary gas mixture's Nusselt and Reynolds numbers:

$$X_{He} = f(Nu_d, Re_d) \quad (2.5)$$

This principle also applies to the concentration probe used in supersonic flows as the hot-film CTA system is still the key component of the probe and operating in a subsonic flow environment inside the probe. For the concentration probe developed for supersonic flow applications, the hot-film is located at the probe's plenum chamber where static conditions are more than 99.5% of the total conditions. Using the inviscid, adiabatic, quasi-one-dimensional analysis, flow conditions impinging on the hot-film are shown in figure 2.2.

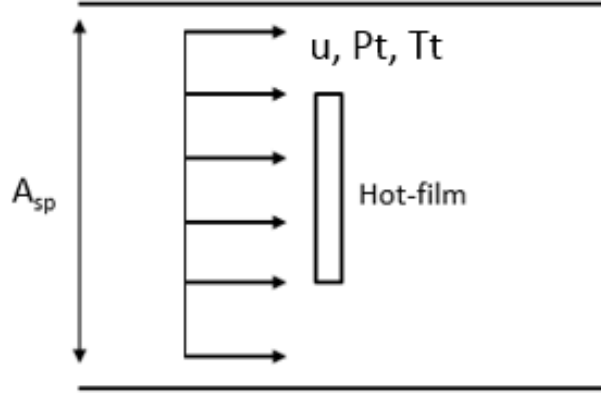


Figure 2.2 Schematic of the hot-film in the sensing plane with uniform flow assumption.

Inside the probe, the hot-film is measuring the average mass flux impinging on it. Due to the uniform flow assumption, the average mass flux impinging on the hot-film equals the average mass flux impinging across the entire sensing plane A_{sp} . As the flow is choked at the throat, the measurement by the hot-film can be rewritten as equation (2.6):

$$\bar{\rho}u = \frac{\dot{m}}{A_{sp}} = \frac{P_t C^* A^*}{\sqrt{T_t} A_{sp}} \quad (2.6)$$

where A_{sp} is the internal cross-sectional area of the probe housing the hot-film, subscript t and superscript $*$ denotes the choking and sonic condition at the throat, respectively, where C^* is defined as:

$$C^* = \sqrt{\frac{\gamma}{R}} \left(\frac{2}{\gamma+1} \right)^{\frac{\gamma+1}{2(\gamma-1)}} \quad (2.7)$$

This average mass flux in equation (2.6) gives the Reynolds number using the hot-film's diameter as the reference length:

$$Re_d = \frac{\bar{\rho}u d}{\mu} = \frac{P_t C^* A^* d}{\sqrt{T_t} A_{sp} \mu} \quad (2.8)$$

Because the hot-film is in conjunction with a CTA system to maintain a constant temperature, the heat transfer of the hot-film is balanced between the heating of the electric

current, equation (2.9), and the cooling of the surrounding fluid, equation (2.10):

$$\dot{Q}_h = I_f^2 R_f = \left(\frac{V}{R_f + R_s}\right)^2 R_f \quad (2.9)$$

$$\dot{Q}_c = hA(T_f - T_t) = Nu_d \pi k l (T_f - T_t) \quad (2.10)$$

where V is the CTA output voltage, R_f is the film's resistance, R_s is the resistance in series with the hot-film, Nu_d is the Nusselt number using the hot-film's diameter as the reference length, k is the thermal conductivity of the impinging fluid, l is length of the film, T_f is the temperature of the film and T_t is the temperature of the impinging fluid. Here, the total temperature T_t of the fluid is used because the sensors are located at the plenum chamber where the static condition is essentially the total condition. From the heat transfer property, the Nusselt number can be related to the output CTA voltage by equation (2.11):

$$Nu_d = \frac{V^2 R_f}{\pi k l (T_f - T_t) (R_f + R_s)^2} \quad (2.11)$$

A power law relation exists between the mixture's Nusselt number and Reynolds number, known as King's law. However, a more widely used modified version is developed by Devillers and Diep in 1972 [3], expressed as (2.12):

$$Nu_d = a(Re_d)^b \quad (2.12)$$

where for an air-helium mixture, a and b are functions of the helium concentration only and are determined from the calibration of the probe.

At this point, by combining equations (2.8), (2.11) and (2.12), and rearranging terms gives the final governing equation for the composition measurement of a binary gas mixture:

$$a\left(\frac{P_t C^*}{\sqrt{T_t}} \frac{A^*}{A_{sp}} \frac{d}{\mu}\right)^b = \frac{V^2 R_f}{\pi k l (T_f - T_t) (R_f + R_s)^2} \quad (2.13)$$

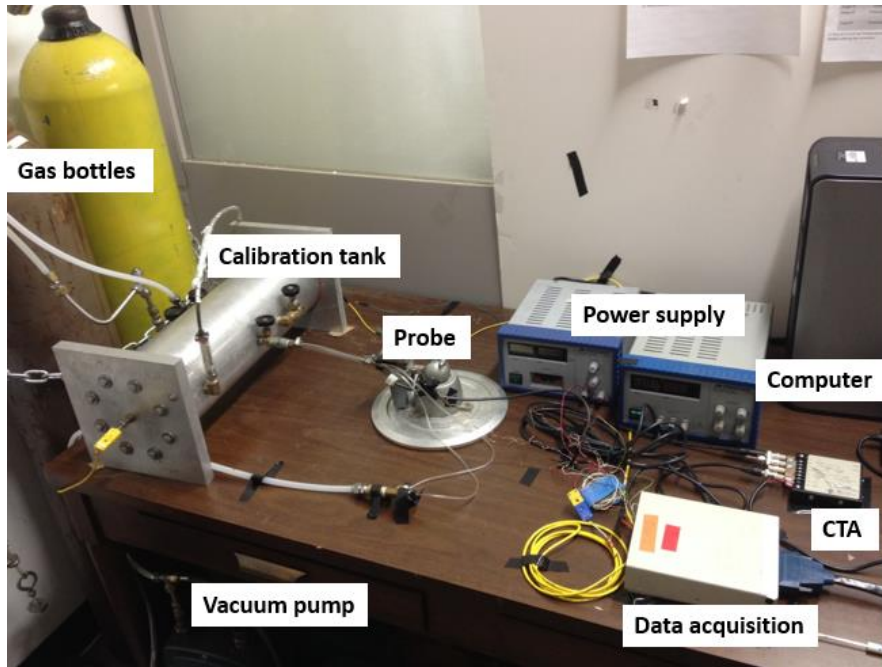
In equation (2.13), A^* , A_{sp} , d , R_f , R_s and l are design constants; P_t , T_t and V are measured variables; a and b are empirical constants for different helium concentrations; and k , C^* , μ are functions of the helium concentration X_{He} . Thus, the helium concentration X_{He} is implicitly included in the governing equation (2.13) and is only a function of the measured total conditions and output CTA voltage for a concentration probe.

2.3 Probe Calibration

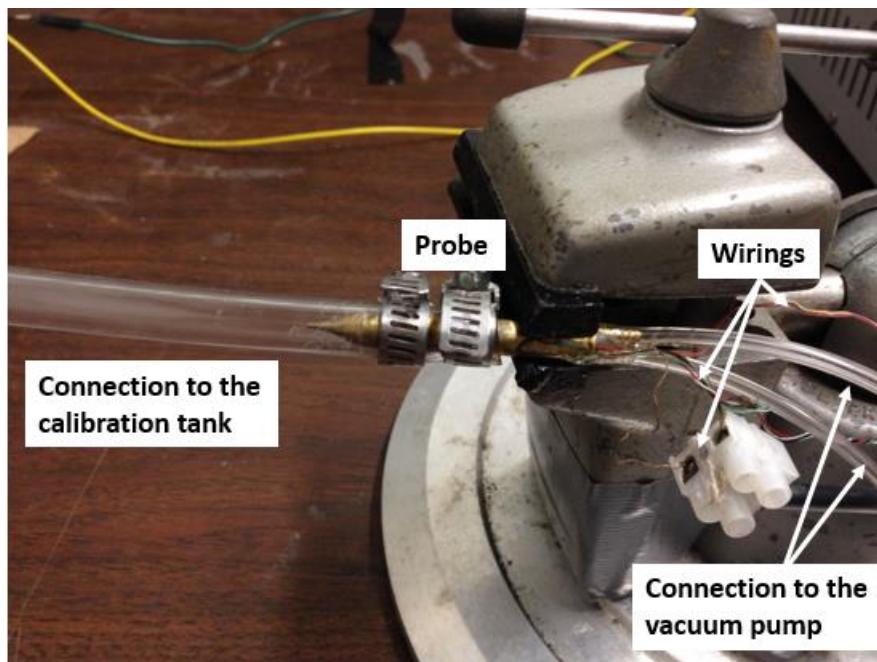
As the helium concentration X_{He} is implicitly included in the governing equation, a calibration of the probe is needed in order to find the empirical constants a and b so that the unknown helium concentrations in the wind tunnel experiments can be determined. Detailed operation procedures can be found in reference 5.

The essential operation of the calibration is performed by placing the probe inside a calibration tank that is filled with a mixture of known helium-air composition. While relieving the mixture inside the calibration tank through the probe with a vacuum pump, the total pressure inside the probe's plenum chamber and the CTA voltage are recorded to form a calibration curve at the calibration temperature by a least squares fitting. This process is repeated for multiple mixtures of different helium concentrations. Then constants a and b for each helium concentration can be found through equation (2.12). In addition, since the total temperature measured during the wind tunnel tests can be different from the total temperature during the calibration process, the temperature corrected calibration

curves are needed for accurate measurements and can be made once a and b are known. A setup of such calibration using the probe in this study is shown in figure 2.3.



(a)



(b)

Figure 2.3 Calibration setup (a) the overall setup (b) a close look on the probe.

Finally, the mixture composition in the wind tunnel tests can be found by linearly interpolating the measured total pressure and CTA voltage onto the temperature corrected calibration curves. A set of such calibration curves from the experiment is shown in figure 2.4. The non-intersecting calibration curves prove the uniqueness of the composition based on the measured total pressure P_t , total temperature T_t , and CTA output voltage V .

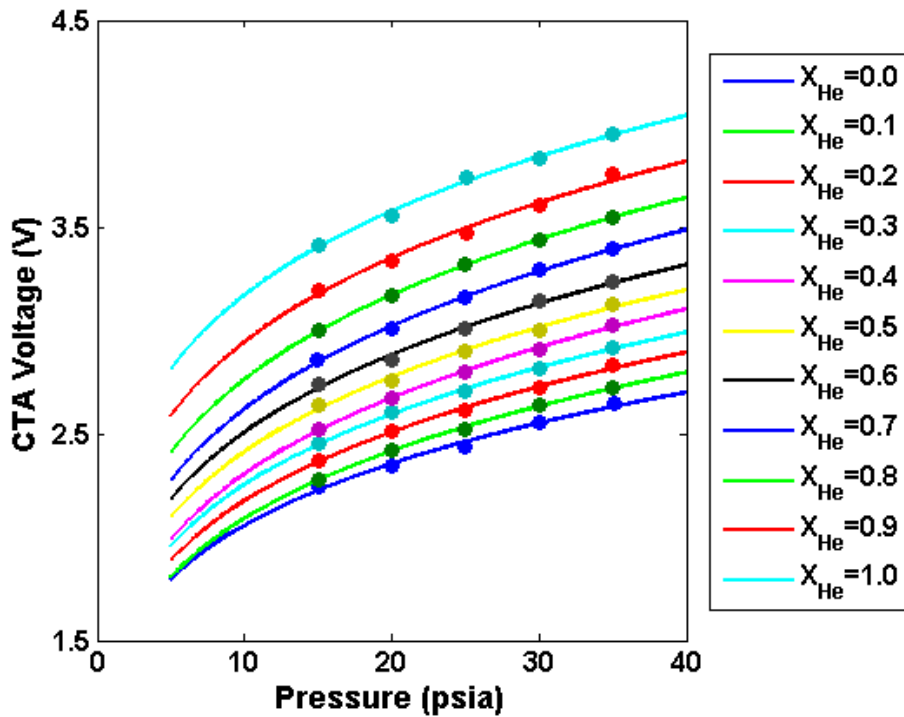


Figure 2.4 Example of calibration curves from a calibration operation.

Chapter 3

Characteristics of the Current Probe

In chapter 2, the generic design of the probe is used to explain the operating principle and the internal gasdynamics. In this chapter, a more detailed discussion is centered on the current probe used at the ARC, which was designed by Wiswall in 2013. Same as in chapter 2, the characteristics of the probe are analyzed based on an adiabatic, inviscid quasi-one-dimensional analysis except a three-dimensional conical flow analysis is used for the external gasdynamics of the probe in section 3.3.

3.1 Details of the Probe Considered in Current Study

The probe in this study was designed by Wiswall in 2013. It adopted the advantages of several designs from previous applications. To be more specific, it follows the idea of Ng's probe but integrates three sensors inside the probe to improve the testing efficiency and frequency response. The probe integrates a TSI 1276-10A hot-film in conjunction with a TSI 1750A CTA, a subminiature Kulite XCQ-062-50A pressure transducer and an Omega Type-K thermocouple. In order to house these sensors, the probe has a large plenum chamber and two symmetrically placed throats.

The difference between this probe design and the generic architecture is shown in figure 3.1. The differences include (a) a straight inlet (section 1) is added to straighten the sampling flow for any freestream flow angularities; (b) a constant section housing the hot-

film (section 3) is added to make the hot-film closer to the probe tip (instead of housing the hot-film at section 5), therefore decreasing the mixture's residence time before impingement on the hot-film in order to limit the negative effect of the internal-occurring mixing; and (c) a second diverging section (section 4) is added to further decrease the flow velocity and to allow sufficient space for installing the thermocouple and pressure transducer in section 5.

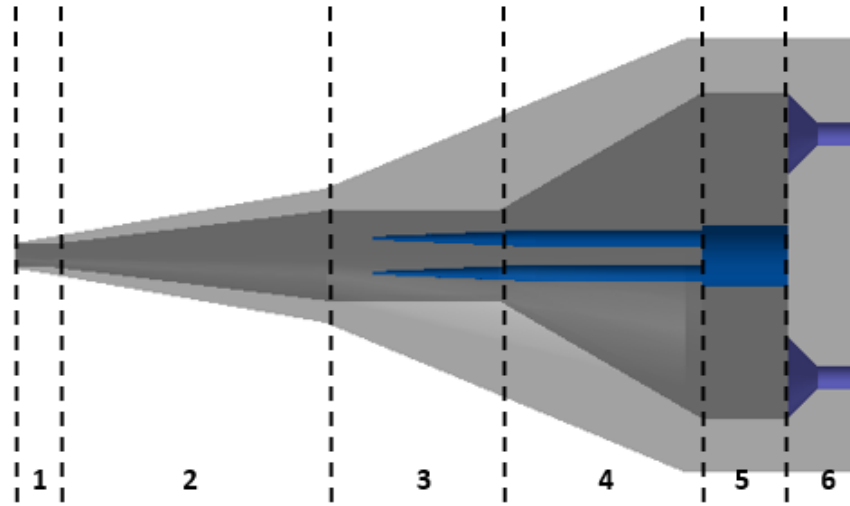


Figure 3.1 2D schematic of the two-throat probe used in this work.

For the hot-film and CTA system, an over-heat ratio (OH) of 1.56 and control resistor of 39Ω are chosen so that the hot-film's operating temperature is about 247°C according to equation (3.1).

$$OH = \frac{R_H}{R_C} = \frac{R_C[1+\alpha(T_H-T_C)]}{R_C} \quad (3.1)$$

where R_H is the resistance of the hot-film at the operating temperature T_H , R_C is the resistance of the hot-film at the ice point temperature T_C , and α is the temperature

coefficient of resistance.

For the total temperature measurement, the initial thermocouple Wiswall planned to install was an Omega CHAL-0005 type-K thermocouple, but the actual thermocouple installed was an Omega 24 AWG type-K thermocouple with a dynamic compensation [5]. This resulted in a slower thermocouple response than the initial plan. The frequency response characteristics of the probe are discussed in section 3.4.

3.2 Characteristics of the Probe's Internal Gasdynamics

In this section, the two-throat probe is analyzed based on the inviscid, adiabatic, quasi-one-dimensional analysis discussed in section 2.1. Despite one of the throat in the physical probe was sealed by Wiswall during previous operations [5], the two-throat probe is studied for the reason of the original two-throat structure designed for better flow straightening capability. In order to be consistent between the CFD study and the actual probe experiment, the physical probe was repaired to have two throats again and tested in this work.

From previous wind tunnel experiments which the injector was injecting air, it is found that the flow conditions at the probe's sampling plane (10h downstream from the injector) have a Mach number ranging from 1.2 to 2.2 and total pressure from 129.8 to 519.2 kPa [8]. The same freestream flow conditions are assumed in this work when investigating a pure helium case.

As mentioned in section 2.1, with the freestream flow conditions and probe geometry, the inviscid, adiabatic, quasi-one-dimensional analysis allows flow conditions along any

axial locations inside the probe to be known. A Matlab code is created based on this analysis and is listed in Appendix A.1. In figure 3.2, the Mach number and cross-sectional area along the internal length of the studied probe for $M_\infty=2.2$ are shown. The flow is shown to go through a supersonic expansion, a normal shock, a subsonic expansion and finally reaches Mach 1 at the throat. In addition, figure 3.3 and figure 3.4 show the ratio of static conditions over stagnation conditions along the probe. It is shown that the normal shock is trapped within the first diverging section; and static conditions are more than 99.5% of the total conditions at the probe's plenum chamber section so they can be used to represent the total conditions; and no mixture liquefaction will occur under these flow conditions.

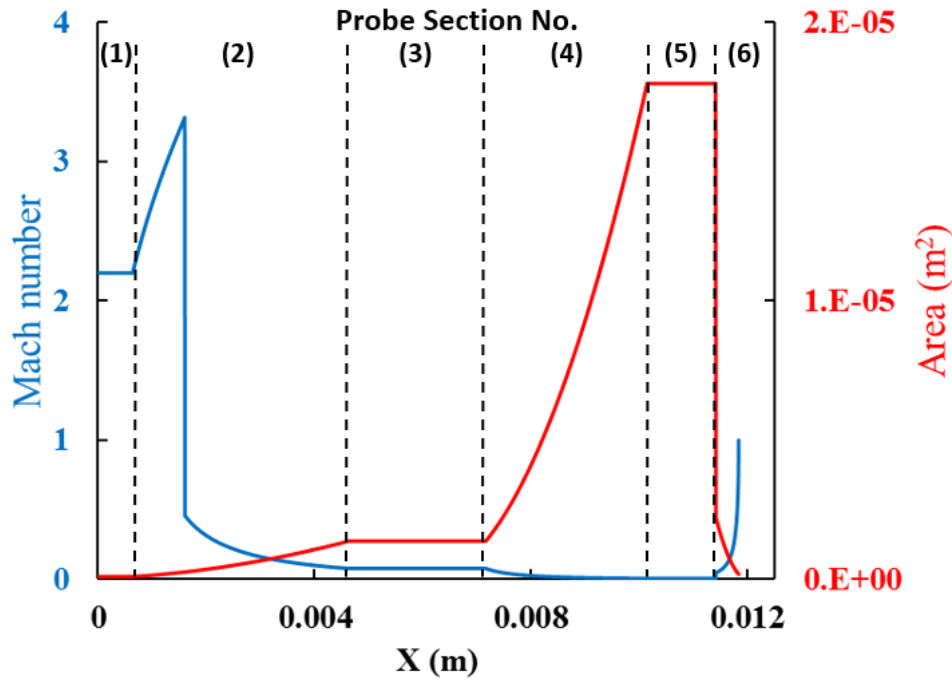


Figure 3.2 Mach number and cross-sectional area along the internal length of the studied probe for $M_\infty = 2.2$.

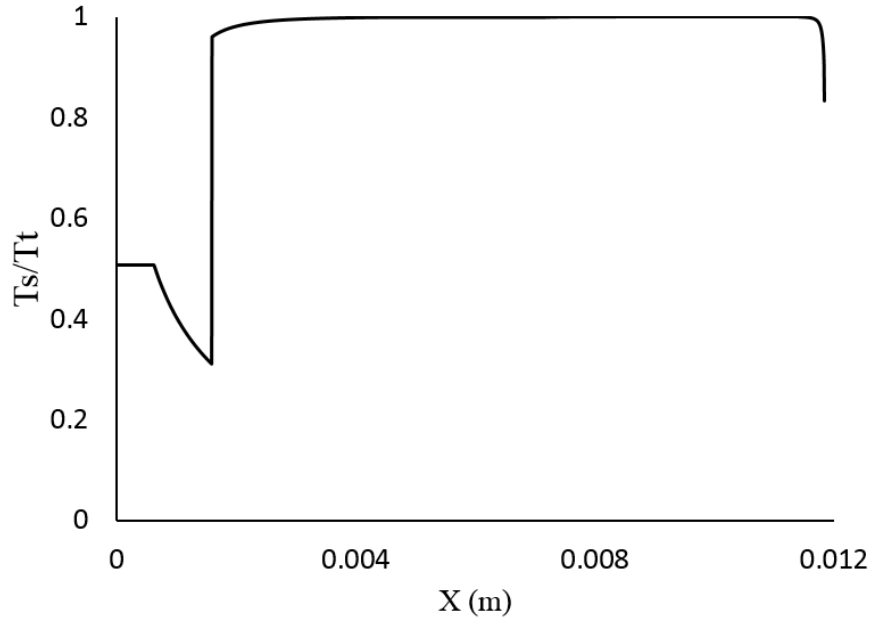


Figure 3.3 Ratio of static temperature over total temperature along the probe for $M_\infty = 2.2$.

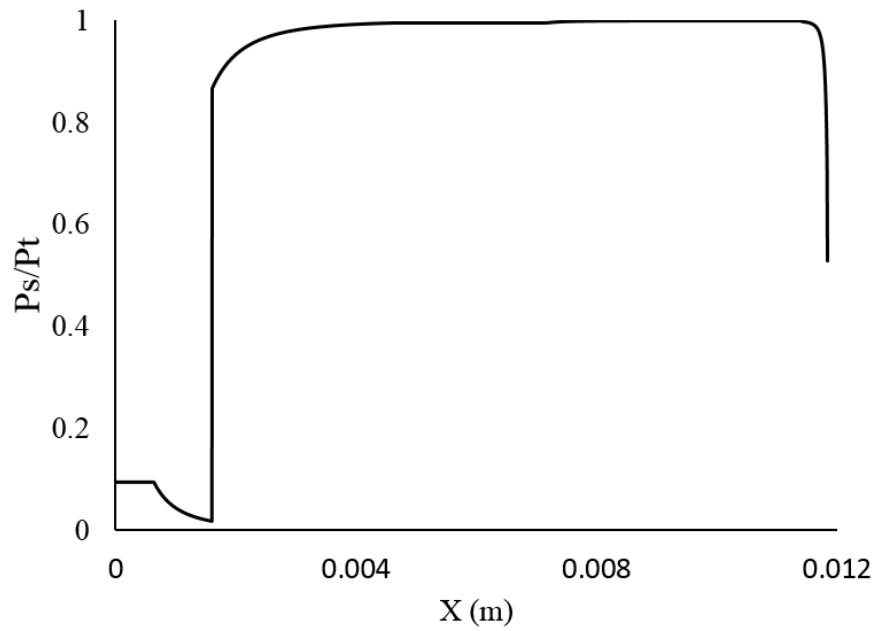


Figure 3.4 Ratio of static pressure over total pressure along the probe for $M_\infty = 2.2$.

In table 3.1, characteristics of the internal gasdynamics for the current two-throat probe of the experimentally measured Mach number and total pressure range at the sampling plane are listed. In table 3.1, the normal shock is found to be always located within the first diverging section and its location is shown as percentage of the axial length of the first diverging section.

Table 3.1 Characteristics of the current probe based on the inviscid quasi-one-dimensional analysis.

Freestream Composition	M_∞	$P_{t,\infty}$ (kPa)	Mach Number in front of Shock	Normal Shock Position (%)
Pure Air	1.2	129.8	2.53	21.94
Pure Air	2.2	519.2	3.32	24.18
Pure Helium	1.2	129.8	2.78	20.68
Pure Helium	2.2	519.2	3.67	21.98

3.3 Characteristics of the Probe's External Gasdynamics

To ensure the isokinetic sampling of the flow, it is crucial to select a probe geometry that minimizes the chances of the external shock detaching at the probe tip under various testing conditions. Since freestream flow is supersonic, this means the design should avoid a detached shock forming at the probe's tip. However, an attached oblique shock will only form along the probe's external wall under restricted conditions. Either the probe's tip angle can be too large to maintain an attached shock for the freestream Mach number or the

freestream flow angularity can be too large for the shock to stay attached. To avoid a detached shock, the probe's tip angle should be designed to satisfy the Taylor-Maccoll relation for conical flows. Table 3.2 shows the allowable freestream flow angularity for the attached shock of the two extreme gas compositions and Mach numbers the probe is expected to experience at 10h. The probe was designed with a tip angle of 10° .

It is shown in table 3.2 that no shock detachment would occur for the current probe design if the probe is aligned with the freestream flow. However, flow angularities are expected in vortex-dominated flows where the probe is sampling. It is shown that the smallest allowable flow angularity that could initiate a detached shock is when the flow is sampling a pure helium gas with a Mach number of 1.2. In other scenarios, the probe can handle the detachment up to a flow angularity of about 33° . In this analysis, the allowable flow angularity and freestream Mach number restrict the applicability range of the current probe.

Table 3.2 Allowable flow angularity for attached shock under freestream conditions.

Gas	Mach	Maximum	Probe Tip	Allowable Flow
Composition	Number	Cone Angle	Angle	Angularity
Pure Air	1.2	19.46°	10°	9.46°
Pure Air	2.2	43.22°	10°	33.22°
Pure Helium	1.2	18.31°	10°	8.31°
Pure Helium	2.2	39.24°	10°	29.24°

While table 3.2 shows the allowable flow angularity for the two extreme gas compositions and Mach numbers, figure 3.5 shows a full three-dimensional plot of the maximum allowable flow angularity among the possible freestream gas compositions and Mach numbers at 10h. In figure 3.5, the colored surface shows the critical flow angularities that the shock detachment could occur on the probe. Isokinetic sampling is ensured as long as the flow angularity does not surpass this limit. Taylor-Maccoll conical flow is used in this analysis instead of a two-dimensional wedge flow analysis to best reflect the actual three-dimensional external flow behaviors and best predict the working range of the concentration probe.

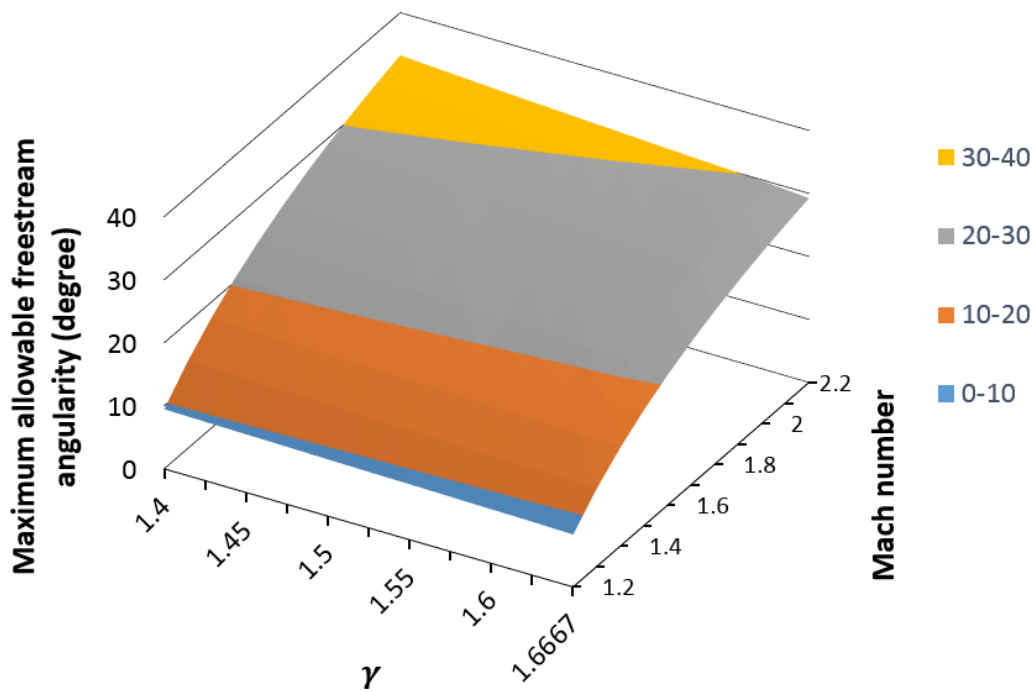


Figure 3.5 Three-dimensional plot of the maximum allowable flow angularities for freestream conditions at 10h.

Besides the analysis above, there is one more factor that will affect the probe's external gasdynamics. The aforementioned analysis on the external flow is assuming a perfect sharp tip so an oblique shock would form. However, the manufacturing could not provide such perfect sharp tip, and the probe tip is more rounded locally so a bow shock will form instead, as shown in figure 3.6. This effect is unavoidable and could affect the actual gasdynamics experienced by the probe. Details of this effect are included in chapter 4 & 5.

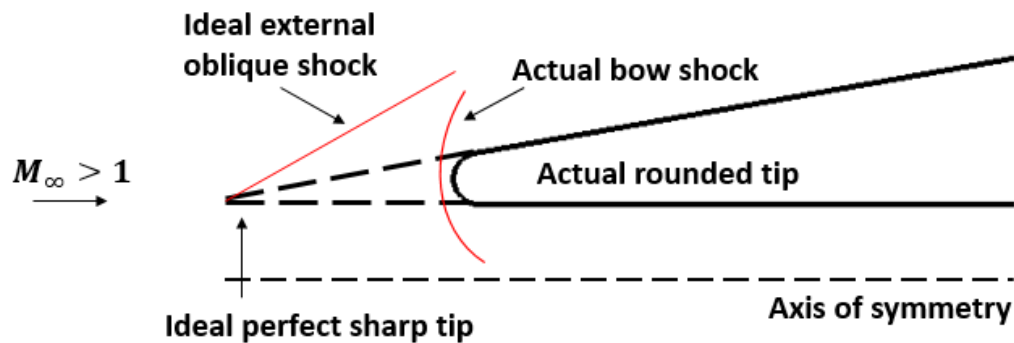


Figure 3.6 Flow at the probe tip of ideal and real cases.

3.4 Frequency Response of the Current Probe

Besides the internal and external gasdynamics of the probe, it is also important to understand the probe's frequency response characteristics for experimental setup and operation. A fast response probe not only could improve the testing efficiency, but also could be used for instantaneous composition measurements.

With the integrated sensors, the current probe's overall frequency response will depend on the frequency characteristics of both the sensors and the probe's internal geometry.

Unlike most of the previous concentration probes, the current probe uses an integrated

miniaturized pressure transducer instead of a pressure tap. In addition, it integrates a thermocouple to avoid additional experiments of the total temperature measurement. These integrations greatly improve the frequency response of the probe and the testing efficiency (more measurements in one wind tunnel run). However, the integrations require a careful selection of sensors and add on more restrictions on the design of the probe's internal geometry to house these sensors.

For the three sensors used in this probe, the frequency response of the CTA system comes from the manufacturer and have a frequency of 100 kHz [10]. The actual frequency response of the hot-film in conjunction with the CTA system was measured by Wiswall to be around 60 kHz [5]. Like the CTA system, the frequency response of the pressure transducer XCQ-062-50A also comes from the manufacturer and the natural frequency is typically 300 kHz without screen.

Unlike the CTA and pressure transducer, the thermocouple's frequency response depends on the operating environment and is provided by the manufacturer for selected flow conditions. However, the thermocouple is a first-order instrument so its time constant can be calculated from its transfer function [11]. To summarize, the thermocouple's response depends on the sensing element's thermal inertia equated with the forced heat convection of the surrounding medium. By assuming a lumped heat transfer on the sensor, the energy equation can be simplified to equation (3.2):

$$mC \frac{dT_{TC}}{dt} = hA(T_{TC} - T_{\infty}) \quad (3.2)$$

where mC is the thermal inertia of the thermocouple, h is the heat transfer coefficient of

the fluid, A is the area of the sensing element, T_{TC} is the temperature of the sensing element, and T_{∞} is the temperature of the impinging fluid. Rearranging into the standard form and taking the Laplace transform yields the thermocouple's transfer function as the following:

$$\frac{T_{TC}(s)}{T_{\infty}(s)} = \frac{1}{\left(\frac{mC}{hA}\right)s+1} = \frac{K}{\tau s+1} \quad (3.3)$$

where the time constant τ is experimentally determined by the vendor for a specific heat transfer coefficient, which strongly depends on the velocity and fluid impinging on the sensing element. The current probe was originally designed to use an Omega CHAL-0005 type-K thermocouple but eventually a 24 AWG type-K thermocouple plus dynamic compensation was used. It has a final response time of 0.6 s given by Wiswall [5]. A summary of the frequency response of the sensors used in this probe is listed in table 3.3.

Table 3.3 Summary of characteristics of the sensors used in the probe.

Sensors	Model	Frequency Response
CTA	TSI 1750A	100 kHz
Pressure transducer	Kuilte XCQ-062-050A	300 kHz
Thermocouple (planned)	Omega CHAL-0005	≈ 1 kHz
Thermocouple (actual)	24 AWG type-K	≈ 1.67 Hz

Besides the sensors inside the probe, the probe's internal geometry determines how fast the fluid could fill it up. By using the inviscid, adiabatic, quasi-one-dimensional analysis tool in appendix A.1, it is able to acquire velocities at each discrete length inside the probe for a given temperature, and thus allow the time to fill up the probe (from the

inlet to the throat) to be determined. This fill time is calculated by summing the discrete time period required for flow to travel the discrete length along the probe. This parameter is essential in choosing the right measurement data as it takes the fill time for a new mixture to be determined when probe sampling position is changed within a single wind tunnel operation.

Another important characteristic of the frequency response is the flush time of the probe, which is the time required for a fluid particle to travel from the sensor plane (where the hot-film sensing element is taking measurement) to the choked throat. This time is important since the mass flow rate inside the probe is governed by the choked flow at the throat and the hot-film sensing plane should feel the same mass flow rate. Thus, the mixture within a flush time is essentially identical. This important parameter is used to determine how long the probe should stay in one sampling position, and gives how many collected data for mean composition measurement at a single sampling position. Same as the fill time, velocities can be found along the probe and the flush time is calculated by summing the discrete time period for travelling the discrete length from the hot-film to the throat.

The probe's fill time and flush time for the pure air or pure helium flow are listed in table 3.4. In table 3.4, Mach number is not specified because it is found that negligible difference exists in the fill time and flush time for the freestream Mach number range the probe is expected to experience.

Table 3.4 Fill time and flush time of the probe operating at 20°C.

Gas Composition	Fill Time (ms)	Flush Time (ms)
Pure Air	1.44	1.35
Pure Helium	0.50	0.47

The overall frequency response of the probe depends on the mixture conditions at the sampling locations. It is composed of the time needed for the flow to reach the sensors first plus the time needed for the sensor to record the new inputs. Since the hot-film CTA system and the pressure transducer has a frequency response about two order of magnitude faster than the thermocouple and the probe's fill time, the overall frequency response of the probe is restricted by the fill time and the thermocouple. Therefore, it is found that the slowest case is for pure air flow and the final overall frequency response of the probe in this work is estimated to be 1.7 Hz for the currently installed thermocouple. This frequency response, however, could be greatly improved by using a faster thermocouple.

Chapter 4

Computational Models and Methods

The concentration probes previously developed are based on the inviscid, adiabatic, quasi-one-dimensional analysis described in section 2. However, viscous effects could affect the desired flow characteristics inside the probe because the probe is sampling a high total pressure supersonic flow with shockwave interactions. Previous wind tunnel experiments using the current probe gave erroneous composition measurements from the freestream conditions. This led to the questioning of its performance and if the inviscid quasi-one-dimensional flow accurately reflects the flow structure inside the probe. Since it is not possible to directly observe the internal gasdynamics of this probe, computational fluid dynamics (CFD) is used to examine the internal and external gasdynamics on a full three-dimensional concentration probe including viscous effects.

4.1 Geometry Used in the Computational Domain

The probe geometry used in this CFD analysis is carefully simplified to allow for better meshing and solving capabilities without impacting the internal gasdynamics of interest. The change involves three locations. Firstly, the thermocouple and pressure transducer in the CFD model are neglected. This is because of their small size and incompressible flow at their locations. This simplification helps on cleaning the geometry for better meshing. It also gives the model two planes showing a symmetric geometry while saving the

computational time without greatly altering the flow behavior. The first viewing plane, XY plane, can show the hot-film and the probe's two throats. The other plane, XZ plane, is perpendicular to the XY plane and could show the locations of the pressure transducer and thermocouple installed in the physical probe. Secondly, the solid sensing filament of the hot-film is replaced with a fluid counterpart for mass flow rate study, the details of which are discussed in section 5.3. Thirdly, the tip of the probe is slightly rounded for one tenth of the straight inlet length (an arc with diameter of 0.0025 in.), simulating a more realistic imperfectly sharp tip as discussed in section 3.3. This not only simulates a more realistic tip but also helps in improving the local mesh quality. A transparent isometric view of the solid probe is shown in figure 4.1 to illustrate the trimmed geometry.

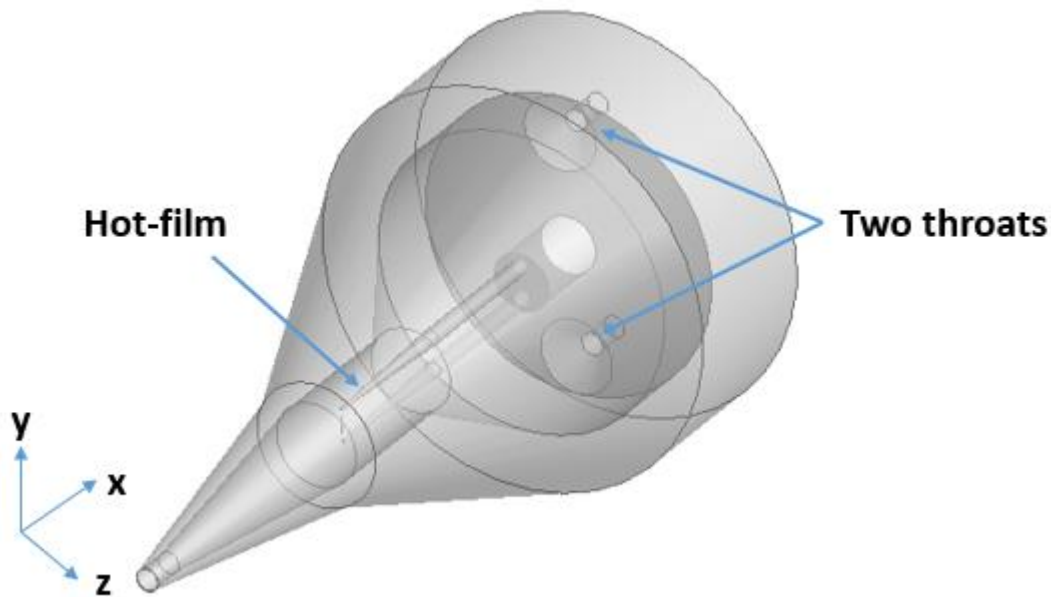


Figure 4.1 A transparent isometric view of the probe.

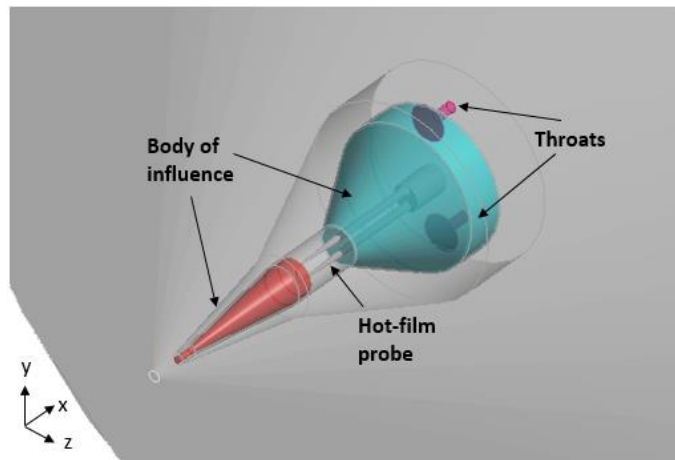
4.2 Meshing Strategy

The computational mesh is generated in ANSYS workbench using an unstructured mesh plus inflation layers. A reentry-vehicle type conical mesh is created around the solid probe to reduce the computational size. This plus the mesh created inside the probe forms the final computational domain.

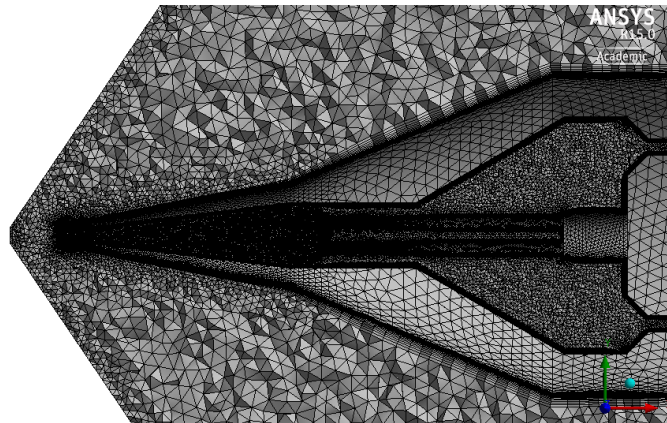
In order to capture boundary layers, the first cell height from the solid wall boundaries is determined based on a value of $y^+=1$. Since the probe has multiple sections with different dimensions and flow conditions, the final first cell height is conservatively chosen by examining the first cell height in all sections and flow conditions for $y^+=1$. Then, the final first cell height is applied globally around the probe. The last aspect ratio method is chosen to create the inflation layers which have 30 levels to ensure that the boundary layer velocity profile is sufficiently resolved and that there is a smooth transition from the inflation layer cells to the unstructured cells.

In addition, local mesh refinement is achieved by using bodies of influence in order to capture the important flow features inside the probe. In the computational domain, two bodies of influence are used at locations where flow properties need to be carefully examined. Namely, the mesh is refined in the first diverging section where the normal shock is expected from the inviscid quasi-one-dimensional analysis; and in the second diverging section where the internal flow decelerates to plenum conditions and total pressure and total temperature measurements are made. The final mesh seen in the XY plane is shown in figure 4.2 with part of the computational domain shown in part (a) and part of the mesh

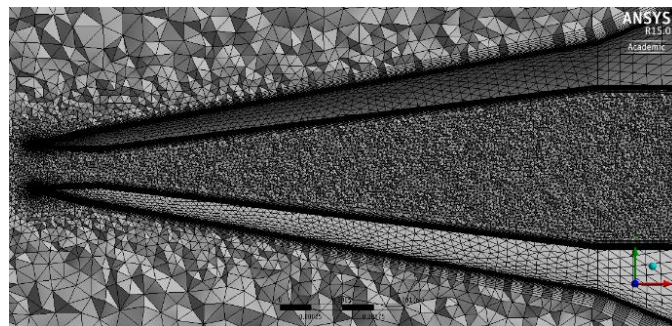
is shown in part (b) and (c) in the whole element form.



(a)



(b)



(c)

Figure 4.2 Meshing strategy (a) the overall computational domain with two bodies of influence highlighted (b) mesh at the XY plane (c) zoomed view around the probe tip.

4.3 Solver Setup

The commercial CFD software ANSYS Fluent is used as the solver. Double precision and 32 parallel processors are used in the fine cases for accurate and fast calculations. In the computational domain, supersonic, subsonic compressible and subsonic incompressible flows will coexist with shock and expansion waves. Thus, the density based solver and Reynolds-averaged Navier-Stokes equations are used to study the concentration probe in steady state. The energy equation is turned on and the SST $k-\omega$ turbulence model is used.

The fluid is modeled as an ideal gas with polynomial equations of viscosity and thermal conductivity as a function of temperature since the static temperature is expected to range from about 50-300 K inside the computational domain based on the quasi-one-dimensional analysis. The equation of viscosity for a binary gas mixture comes from Wilke [12] and the coefficients in the polynomial functions are taken from Fuller [13]. Since the probe could experience compositions ranging from 100% air to 100% helium in the wind tunnel experiments, pure air and pure helium are the two extreme compositions that are studied to give an insight of the probe's gasdynamics.

The boundary condition types in the computational domain is shown in figure 4.3. From the freestream conditions gathered by previous wind tunnel experiments, boundary conditions in the CFD are set up to simulate the conditions the probe is expected to experience. The worst freestream scenario at the sampling plane for the probe's internal gasdynamics is the flow with Mach number of 2.2 and total pressure of 519.2 kPa. This

gives the strongest shock strength and furthest downstream internal normal shock location according to the inviscid quasi-one-dimensional analysis. Thus, this flow condition could have the strongest viscous effects on the probe's gasdynamics and is majorly studied in the CFD for viscous effects. The freestream flow condition is set up as the pressure farfield (input of the Mach number and total pressure), shown in figure 4.3. In addition, static pressure of 20 kPa is extrapolated for the probe's external pressure outlet (the pressure outlet 1). This value will be updated as the flow is supersonic at this location. To simulate the low back pressure condition behind the probe's throats, 300 Pa is extrapolated as the internal pressure outlet boundary condition (the pressure outlet 2). Finally, stationary and no slip conditions are given to the wall. For this adiabatic probe study, zero heat flux is used for the wall condition.

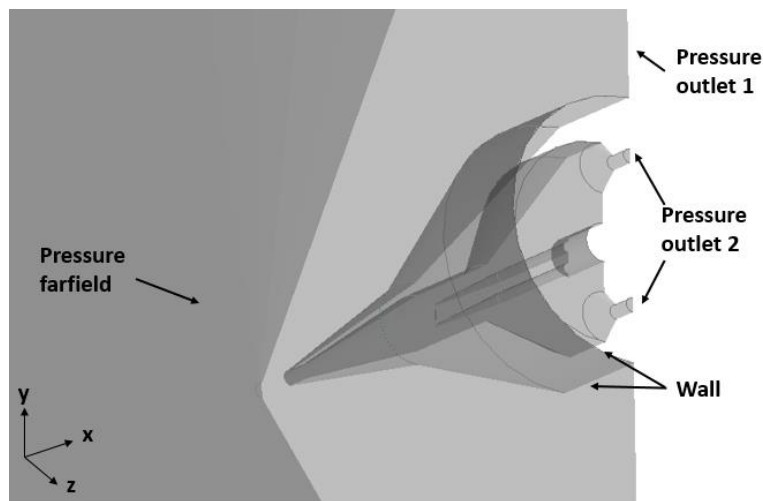


Figure 4.3 Boundary conditions setup shown with a XY-plane cut of the computational domain.

Finally to solve the case, the first-order upwind numerical discretization method was

used to obtain the initial convergence, and then the blending factor was gradually increased up to fully second order discretization. Difficulty was experienced for a fully second order simulation, so a 50% blending factor is finally used. To accelerate the convergence, the Fluent solution steering algorithm is enabled with 5 multi-grid levels in initialization. A Courant number of 0.1 is used for all simulation cases. Table 4.1 lists a summary of the computational settings.

Table 4.1 Summary of the solver settings.

Solver	Type	Density-based
	Time	Steady
Models	Energy Equation	On
	Turbulence	SST k- ω
Materials	Gas density	Ideal Gas
	Gas viscosity	Polynomial
	Thermal conductivity	Polynomial
Boundary Conditions	Pressure farfield	Mach 2.2 air/helium
	Pressure outlet 1	20000 Pa
	Pressure outlet 2	300 Pa
	Wall	Stationary, No-slip, Zero heat flux
Solution	Flux type	AUSM
Methods	Gradient	Green-Gauss node based

Chapter 5

Computational Results and Discussion

This chapter presents the results of the CFD study on the concentration probe under different flow conditions. It mainly focuses on the two extreme gas compositions of the sampled mixture (pure air and pure helium) with various freestream flow angularities for the freestream Mach number and total pressure data gathered at a specific sampling matrix (10h) in previous wind tunnel experiments.

5.1 Grid Independence Study

Figure 5.1 shows the Mach number contour in the XY plane of the computational domain. As it shows, there are two sets of oblique shocks followed by a Prandtl-Meyer expansion wave externally around the probe. Internally, the rounded tip creates shockwave interactions and an oblique shock train is formed in the first diverging section after the supersonic expansion. This oblique shock train is found to be caused by a shock-induced boundary layer separation which cannot be predicted by the inviscid quasi-one-dimensional analysis. The oblique shock train and the boundary layer separation result in a jet that impinges past the first diverging section of the probe to the hot-film filament location where it will affect the hot-film's measurement of the average mass flux. Details of this jet effect onto the hot-film's measurement are analyzed in section 5.3. Finally, the flow becomes choked at the throat. Similar flow structure is also observed for the minimum freestream

Mach number and total pressure of the studied conditions.

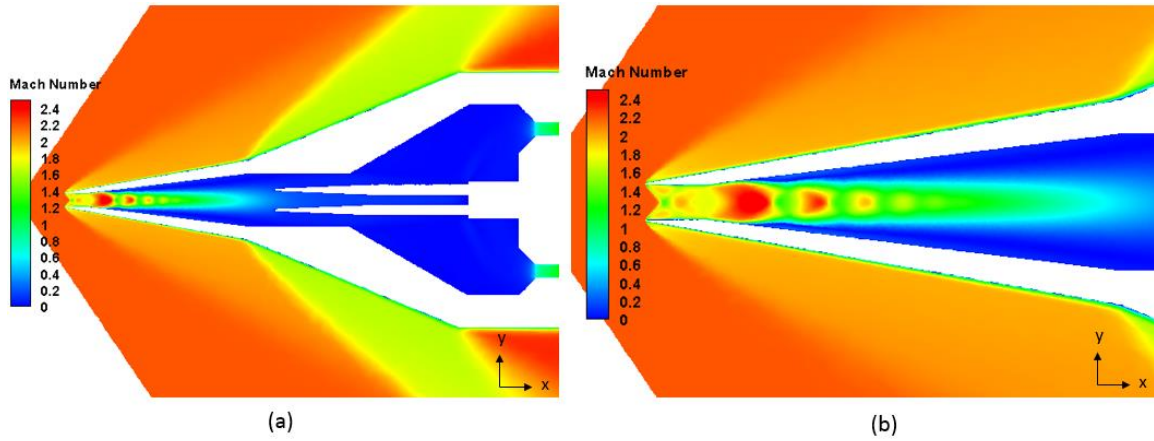


Figure 5.1 Mach number contour (a) in the XY plane (b) zoomed view around the first diverging section.

Figure 5.1 shows the result of a fine mesh case, which comes from a systematic grid independence study. In table 5.1, three levels of mesh used in the grid independence study are listed, namely, the coarse, medium and fine cases. The level of grid is approximately doubled stemming from the coarse case to the medium case, and then to the fine case.

Table 5.1 Mesh information of the grid independence study.

Case	Elements	Nodes
Coarse	2.11M*	0.82M
Medium	4.11M	1.45M
Fine	7.69M	2.54M

*M stands for million

Cases from the coarse grid to the fine grid all show similar flow structures depicted in figure 5.1. However, as the mesh is refined the oblique shock train becomes more highly resolved. As shown in figure 5.2, the difference in the Mach number along the center axis of the probe in crucial locations (such as the oblique shock train) is minimal when the medium and fine meshes are compared. The coarse mesh, however, smears the oblique shock train and does not capture all the subsequent shock/expansion wave reflections. These results, when taken in conjunction with the full results of the grid independence study, allow it to be concluded that the solution of the fine mesh case is grid independent. All subsequent results are presented with solutions on the fine mesh case.

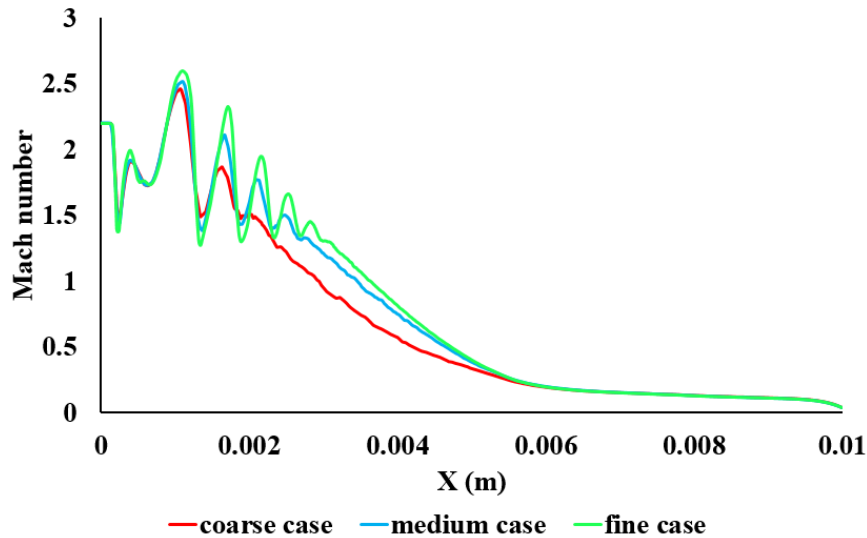


Figure 5.2 Comparison of the Mach number along the axial center of the probe.

5.2 Mean Flow Characteristics of an Adiabatic Probe

As the concentration probe is designed using the inviscid, adiabatic, quasi-one-dimensional analysis, the effects of flow angularities on the probe's internal gasdynamics

are not included. For this reason, the mean flow features of a case without any freestream flow-probe misalignment is used to compare with the flow features predicted by the inviscid quasi-one-dimensional analysis, which the Mach number contour is shown in figure 5.1.

To better observe the flow's shock structure, a Schlieren image is created using the magnitude of the numerical density gradient, shown in figure 5.3. It highlights the boundary layer growth, the external flow features such as the oblique shockwave, as well as the complex shockwave interactions in the tip region of the probe. In addition, the flow inside the probe is characterized by a supersonic expansion when the flow enters the first diverging section and then followed by an oblique shock train. The jet becomes subsonic after approximately four to six sets of oblique shock interactions.

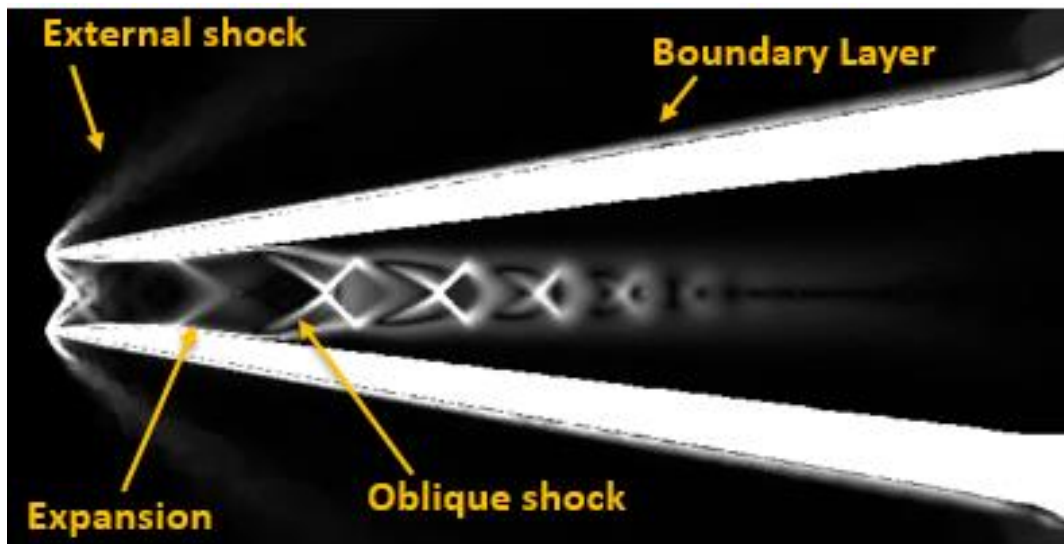


Figure 5.3 Flow visualization by the numerical Schlieren.

In addition, to highlight the internal flow structure affected by the shock-induced

boundary layer separation, streamlines inside the probe in the XY and XZ planes are presented in figure 5.4. In figure 5.4, reversed flows are observed in both the first and the second diverging sections of the probe. In the first diverging section, a shock-induced boundary layer separation is observed. The reversed flow starts to form at the start of the shock formation and the separated flow is observed to reattaches close to the hot-film sensing plane. In the second diverging section, the reversed flow is observed along the wall and recirculation zones are formed. The recirculation zones are different between the XY and XZ planes and most likely are due to the two symmetrically placed throats. In conclusion, with the viscous effects studied in the CFD, it was found that the flow inside the probe does not behave the same way as predicted by the ideally inviscid, adiabatic, quasi-one-dimensional analysis. These viscous effects such as the shock-induced boundary layer separation in the first diverging section and recirculation zones in the probe's plenum chamber could affect the sensors' measurements inside the probe.

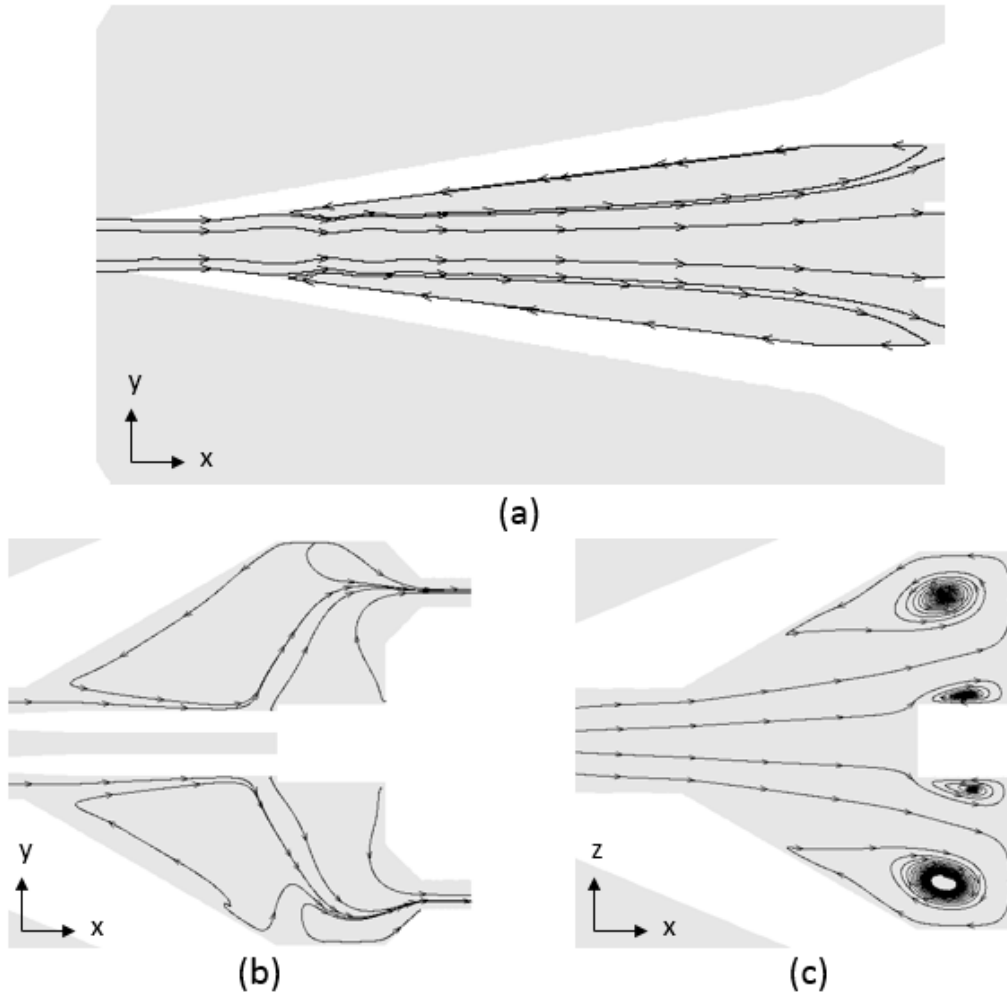


Figure 5.4 Streamlines (a) at the first diverging section in the XY plane (b) at the second diverging section in the XY plane (c) at the second diverging section in the XZ plane.

To verify the results shown above, a boundary layer analysis inside the probe was approached to analyze the viscous effects on the internal gasdynamics. In the inviscid, adiabatic, quasi-one-dimensional analysis, a normal shock is supposed to form in the first diverging section. But according to Chapman [14], if the normal shock is sufficiently strong, it could induce a boundary layer separation due to the large adverse pressure gradient across

the shock. Chapman gives an equation to determine the maximum shock intensity that a boundary layer can withstand without separation, based on the free-interaction theory for $1.1 < M_e < 3.6$, see equation (5.1).

$$C_p = \frac{P - P_e}{q_e} = 0.093[(M_e^2 - 1)Re]^{-1/4} \quad (5.1)$$

To examine if the flow inside the probe could induce a boundary layer separation as shown in the CFD results, equation (5.1) is examined using the predicted values taken from the inviscid quasi-one-dimensional analysis. In table 5.2, $C_{p, \text{critical}}$ is calculated using the right-hand side of equation (5.1) with M_e and Re taken from the inviscid quasi-one-dimensional analysis data, which gives the adverse pressure gradient level when shock-induced boundary layer separation starts. While $C_{p, \text{design}}$ is calculated using P , P_e , and q_e data. A shock-induced boundary layer separation will occur if $C_{p, \text{design}}$ is higher than $C_{p, \text{critical}}$. As table 5.2 shows, a shock-induced boundary layer separation is predicted for the current probe design and operating freestream flow conditions. This result shows consistency with the CFD predictions, proving the accuracy of the computational study and indicating that the inviscid, adiabatic, quasi-one-dimensional analysis does not entirely reflect the current probe's internal gasdynamics.

Table 5.2 Predictions of the shock-induced boundary layer separation.

Gas	M_∞	$P_{t,\infty}$ (kPa)	$C_{p,critical}$	$C_{p,design}$	Induced
Composition					Separation
Pure Air	1.2	129.8	5.94e-3	1.40	Yes
Pure Air	2.2	519.2	3.89e-3	1.52	Yes
Pure Helium	1.2	129.8	6.81e-3	1.31	Yes
Pure Helium	2.2	519.2	4.07e-3	1.39	Yes

Besides the shock-induced boundary layer separation, reversed flow is also observed in the second diverging section. In the second diverging section of the probe, the flow is incompressible and the velocity is decreasing due to the expanding area forming another adverse pressure gradient. The Falkner-Skan method [15] is used to examine the incompressible wedge flow, which represents the scenario similar as the flow in the second diverging section of the probe. For the flow conditions at the second diverging section, the Falkner-Skan method shows that a wedge angle greater than 35.78° is likely to induce a boundary layer separation [16]. This indicates that this probe's design angle of the second diverging section is too large since the current probe has a wedge angle of 60° at the second diverging section. Thus, a boundary layer separation is predicted and is once again consistent with the CFD results.

These two locations of the boundary layer separation shown in the CFD results and verified by the separate boundary layer analysis not only change the probe's internal

gasdynamics but also have the potential to lead to errors in the probe's composition measurements.

Besides the ideal non-freestream-flow-angularity case, which is used in the inviscid, adiabatic, quasi-one-dimensional analysis and in the probe's calibration process, the more common scenario for the probe operating in wind tunnel tests is having various flow-probe misalignments. This is true especially the probe is used to study the mixing effectiveness behind an injector designed to introduce streamwise vortices.

Although the probe geometry is chosen to minimize the chances of the shock detaching at the probe tip under various testing conditions, the unavoidable freestream flow angularities could affect the internal gasdynamics that is neglected in the inviscid quasi-one-dimensional analysis. Therefore, the effect of freestream flow angularities on the internal gasdynamics of the probe must be investigated.

In this computational study, 5° and 10° freestream flow angles of attack (AoA) in the XY plane are examined for both pure air and pure helium cases with the identical freestream Mach number and total pressure as the non-freestream-flow-angularity cases, shown in figure 5.5. In figure 5.5, it is shown that flow angularities caused the "bending" of the oblique shock train and the jet, and the added straight inlet section failed to straighten the flow in such scenarios. To avoid numerical error accumulated in an unstructured mesh that could affect the results, cases of opposite angles of attack are also examined. The results show an opposite inclination of the "bending" of the jet, which confirms the "bending" of the jet is a physical phenomenon not caused by the numerical effects due to

the unstructured mesh.

As shown in figure 5.5, the biggest influence of the freestream flow angularities to the internal gasdynamics is the “bending” of the oblique shock train and the jet. The results show that a larger flow angularity leads to a higher degree of “bending” of the oblique shock train and the jet. For the 10° AoA cases, the jet almost completely leans towards one side of the wall. Since the jet could reach the hot-film’s sensing plane, the condition of the jet will affect the average mass flux measured by the hot-film. Thus, the effect of flow angularities on the measurement of mixture composition needs to be examined and is discussed in the subsequent section.

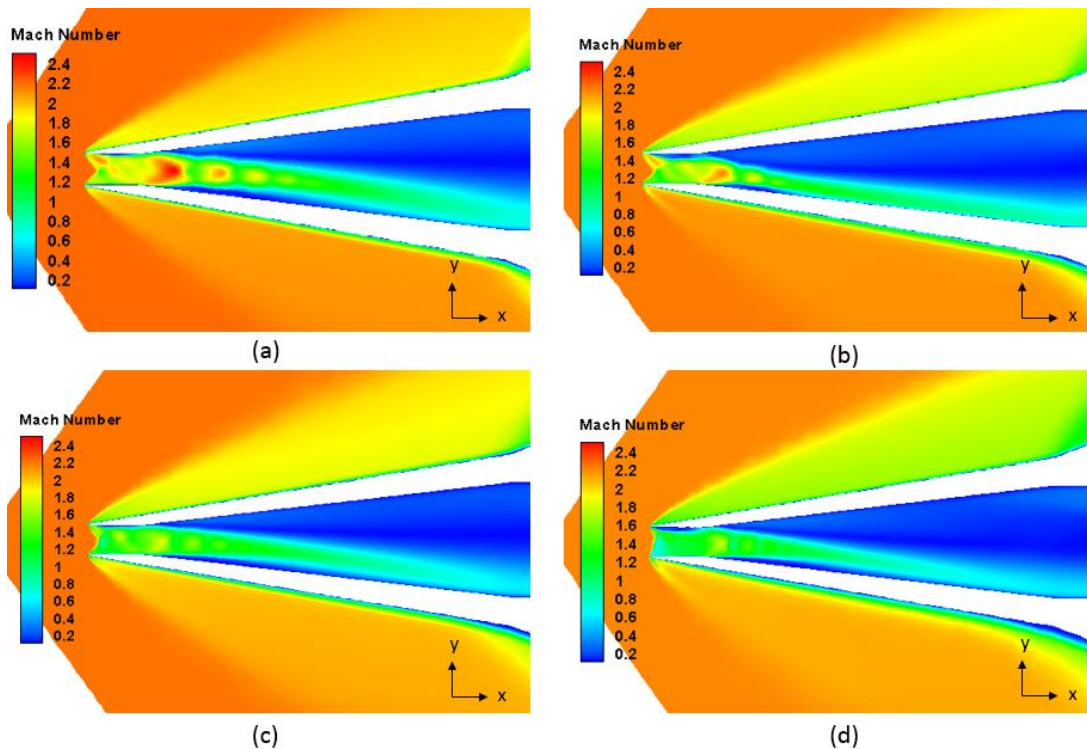


Figure 5.5 Mach number contours in the first diverging section in the XY plane as an effect of the flow angularity: (a) pure air, 5° AoA; (b) pure air, 10° AoA; (c) pure helium, 5° AoA; (d) pure helium, 10° AoA.

5.3 Error Analysis of Helium-Air Composition Measurements

In section 2.2, the governing equation used to find the helium concentration in air-helium mixtures is derived based on a quasi-one-dimensional analysis with the assumption of uniform flows, shown in figure 5.6(a). Therefore, the average mass flux impinging on the hot-film could be substituted with the mass flow rate at the throat (determined by the measurements of the total pressure and total temperature of the choked flow), divided by the sensing plane area, expressed as equation (2.6). This is legitimate because the uniform flow assumption allows the average mass flux measured by the hot-film to be equal to the average mass flux across the entire sensing plane. Then the governing equation could become the form of equation (2.13).

However, this uniform flow assumption is not valid for the current probe operation as CFD simulations show that the jet caused by the shock-induced boundary layer separation impacts the velocity profile along the hot-film's sensing plane. Thus, the average mass flux felt by the hot-film is no longer equal to the average mass flux over the entire sensing plane.

Figure 5.6(b) shows a general example of a non-uniform flow impinging on the hot-film. In the scenario depicted in figure 5.6(b), the average mass flux impinging on the hot-film is higher than the average mass flux of the sensing plane. Thus, despite the choked mass flow rate being identical between the uniform and the non-uniform flow cases depicted in figure 5.6, the output CTA voltage of the hot-film is higher in the non-uniform flow example than the case of the uniform flow. Such difference in average mass flux, if

exist between a viscous case and an inviscid case, will cause error in composition measurements. More importantly, since helium concentrations of unknown air-helium mixtures are found by linearly interpolating the total pressure and the CTA voltage onto the calibration curves, there will be an error in the helium concentration measurement if the average mass flux impinging on the hot-film in a wind tunnel test condition cannot be repeated in its corresponding calibration case, or vice versa.

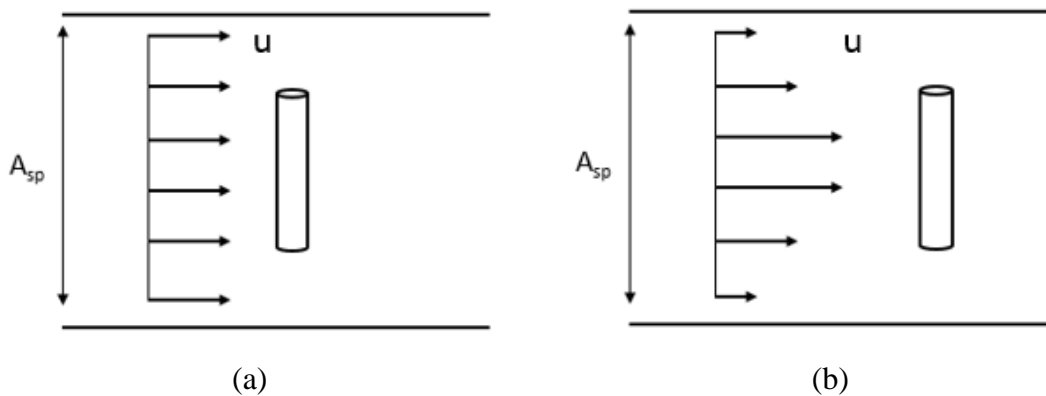


Figure 5.6 Schematic of flows at the sensing plane (a) with uniform flow assumption (b) without uniform flow assumption.

To summarize from the above analysis, there will be no error in the helium concentration measurement only if the measured variables P_t , T_t , and V of a helium concentration X_{He} in the wind tunnel test could be matched with the P_t and V values on the calibration curve of the same X_{He} at T_t . To better visualize the error analysis, an illustrative example using a simplified calibration map is given in figure 5.7. It shows that a flow with P_t and $X_{He,1}$ could give a reading of $V_{He,err}$ instead of V in the wind tunnel test condition because the average mass flux impinging on the hot-film is higher than it is in the

calibration, which leads to an incorrect helium concentration reading $X_{\text{He,err}}$ instead of $X_{\text{He},1}$.

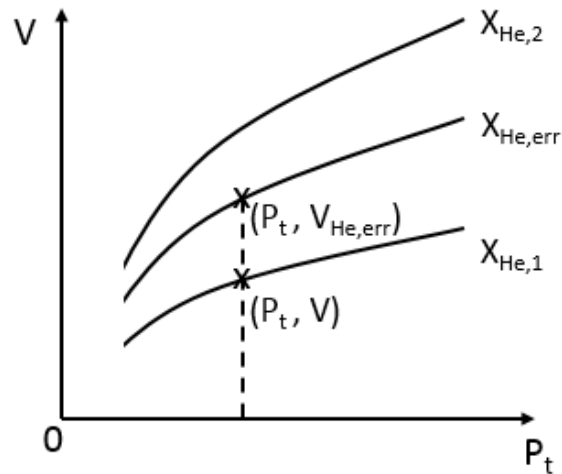
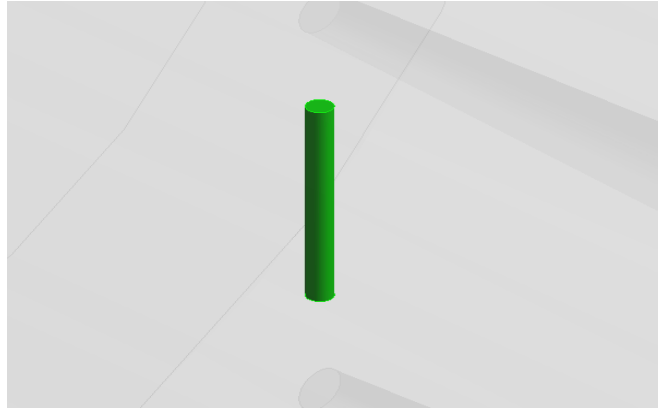


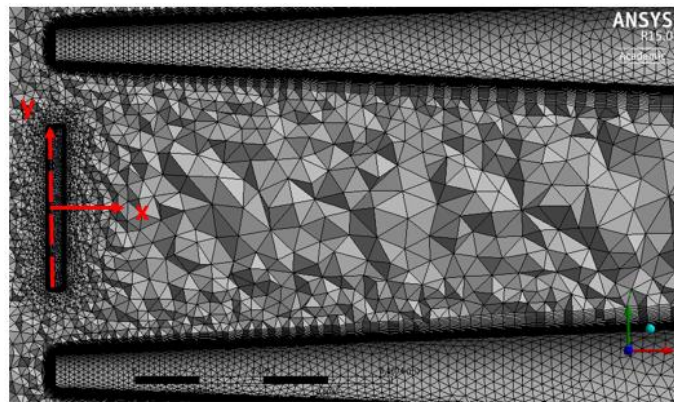
Figure 5.7 Illustration of the error in the helium concentration measurement.

To quantify the error introduced by non-uniform flows over the hot-film sensing plane revealed in the CFD simulations, a separate fluid region is created and meshed in the computational domain to serve as a virtual hot-film filament, see figure 5.8(a). This “hot-film sensing filament” is meshed in a way that structured mesh and computational nodes are on the surface of the filament, as shown in figure 5.8(b). Then in the post processing, the surface of this domain facing the incoming fluid is used to sample the mass flow rate impinging on the hot-film.

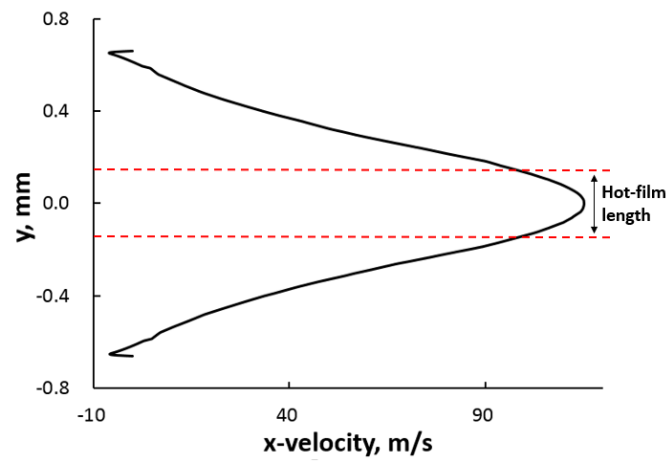
In figure 5.8(c), velocity profile upstream of the hot-film along the entire hot-film sensing plane for pure air zero angularity case is shown with the emphasis of the filament length. It is clearly shown that the average mass flux impinging on the hot-film is not equal to the average mass flux in the entire sensing plane, which is the case discussed using figure 5.6.



(a)



(b)



(c)

Figure 5.8 Mass flow rate measurement (a) “hot-film” element (b) meshing around the “hot-film” (c) velocity profile along the sensing plane in the pure air 0° AoA case.

To numerically check if the internal flow in the CFD of the wind tunnel test conditions would result in the correct reading of mixture's helium concentration from the corresponding calibration curves, a factor F is defined in equation (5.2). F is a ratio of the mass flow rate impinging on the hot-film \dot{m}_f over the mass flow rate at the choked throat \dot{m}_t , where \dot{m}_f is related to the measured CTA voltage and \dot{m}_t is related to the measured total pressure inside the probe plenum chamber. In the inviscid quasi-one-dimensional analysis, the F factor could be substituted by the area ratio A_f/A_{sp} , where A_f is the projected area of the surface of the filament facing the impinging fluid. This gives F factor a value of 4.71×10^{-3} in the inviscid quasi-one-dimensional analysis. The same surface is used for the calibration data and CFD results. From the calibration data, the average F value for the two-throat probe of eleven different concentrations is found to be 7.11×10^{-3} .

$$F = \frac{\dot{m}_f}{\dot{m}_t} = \frac{\dot{m}_f}{\dot{m}_{sp}} \quad (5.2)$$

Table 5.3 lists the data sampled from the CFD results of the two studied compositions and three freestream flow angularities, respectively. The F factor is found through the method mentioned above. In addition, CFD results are used to produce the CTA voltage and the total pressure at the probe's plenum chamber so that the last column in table 5.3 is then calculated based on the actual calibration curves.

For the perfectly flow-probe alignment cases, the F factor is found to be higher in the wind tunnel experiment environment than that in the calibration. This is due to the jet and viscous effects creating a higher velocity towards the center axis of the probe. Consequently,

the $X_{He,predict}$ in table 5.3 shows the over-prediction of the mixture's helium concentration in these cases.

For the other angularity cases, the “bending” of the jet helped in neutralizing this error in the non-angularity cases. A slower velocity is impinging on the center axis of the probe, which gives a smaller F factor. However, it still creates an error in the helium concentration measurement as it under-predicts the actual freestream mixture's helium concentration.

In conclusion, the non-angularity cases are shown to over-predict the helium concentration because of the jet creating a higher average mass flux impinging on the hot-film. The angularity cases, however, could under-predict the helium concentration due to that the ‘bending’ of the jet allows less average mass flux impinging on the hot-film. Such errors in the helium concentration measurement are consistent with the direct comparisons of the F factors in table 5.3 with the F factor found in the actual calibrations.

Table 5.3 Error in helium concentration measurements.

$X_{He,\infty}$	M_∞	AoA	$\dot{m}_f(\text{kg/s})$	$\dot{m}_t(\text{kg/s})$	$F \times 10^{-3}$	$X_{He,predict}$
0.0	2.2	0°	9.01e-7	4.06e-5	22.19	0.63
0.0	2.2	5°	2.30e-7	4.05e-5	5.68	<0
0.0	2.2	10°	8.36e-8	4.16e-5	2.01	<0
1.0	2.2	0°	3.87e-7	2.08e-5	18.60	>1
1.0	2.2	5°	8.28e-8	2.09e-5	3.96	0.82
1.0	2.2	10°	9.83e-8	2.09e-5	4.70	0.88

The errors found in helium concentration measurements by comparing CFD results with probe calibration data explained the erroneous measurements given by this probe in previous wind tunnel tests. Despite the integrated probe was designed to minimize the internal-occurring mixing effect by placing the hot-film closer to the probe tip, this modification is revealed to affect the sensor's measurement by exposing the hot-film to a highly non-uniform flow due to the severe viscous effects.

Chapter 6

CFD-aided Probe Design

From the CFD results and analysis in chapter 5, it is shown that the original design of the probe could produce large errors in helium-air composition measurements due to viscous effects. The original design of this probe was intended to minimize the probe's internal-occurring mixing effect on the measurement by placing the hot-film as close to the tip as possible, and attempt to improve the probe's frequency response by minimizing the probe's length which results in a large internal diverging angle. These arrangements are shown to affect the accuracy of composition measurements due to the flow separation and forming of a jet. As it's important to have accurate composition measurements, a modified probe geometry based on these findings is used as a testbed to study the proper hot-film location with respect to the probe tip in order to minimize the error in composition measurements. The testbed undergoes both the traditional examination of the adiabatic, inviscid quasi-one-dimensional analysis and the CFD study in this chapter.

6.1 Testbed Based on the CFD Study

From section 5.2 and 5.3, it is found that the shock-induced boundary layer created an oblique shock train and the resulting jet could have an effect on the hot-film sensing plane, creating a large velocity variation within the entire sensing plane and error in composition measurements. To avoid such effect, which is to ensure the hot-film is located in a subsonic

flow field with negligible velocity variation between the wind tunnel experiment and the corresponding calibration, the hot-film should be moved further downstream.

In addition, the reversed flow in the second diverging section shown in figure 5.3 should be avoided. This could avoid artificial drop in total temperature measurements due to the thermocouple sampling inside a recirculation region. The jet effect and the recirculation are the two major issues that could lead to the error in helium concentration measurements shown in CFD results and they need to be fixed.

A testbed probe geometry is created based on the aforementioned analysis and requirements. The probe cap, which is the main functioning part of the probe, is shown in figure 6.1. Section 5 is the probe's plenum chamber highlighted in figure 3.1. The testbed geometry still follows the architecture of Wiswall's design. Two major changes are the length of the probe and angle of the second diverging section. To be more specific, the second diverging section angle is decreased to satisfy the Falknar-Skan wedge flow analysis in order to avoid the incompressible flow boundary layer separation. The change in this angle plus a larger diameter in section 3 could further decrease the flow velocity but leads to an increase in the length of section 2 and section 4. Thus the total length of the testbed probe from tip to throat is increased by about 50% compared to the initial design. For this geometry, the hot-film could be installed anywhere from the start of the second diverging section to a position further downstream by adjusting the length of section 5.

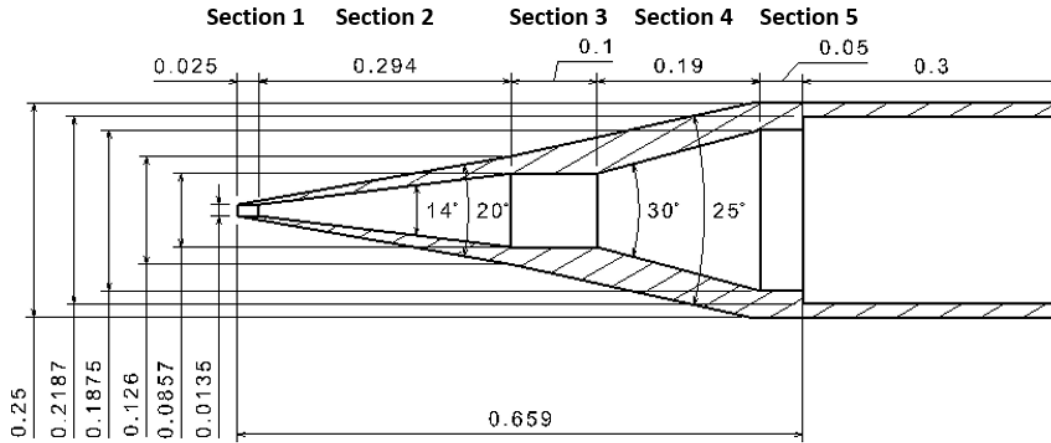
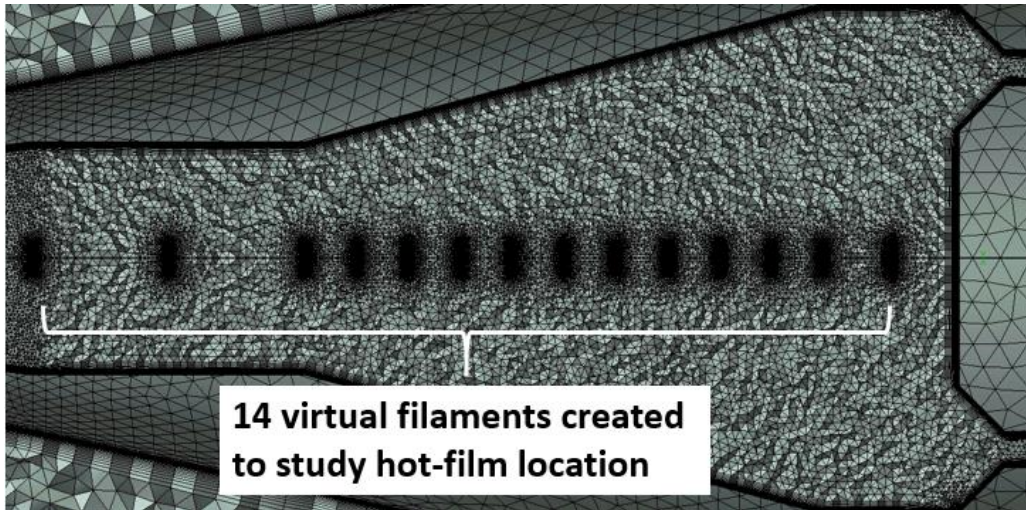


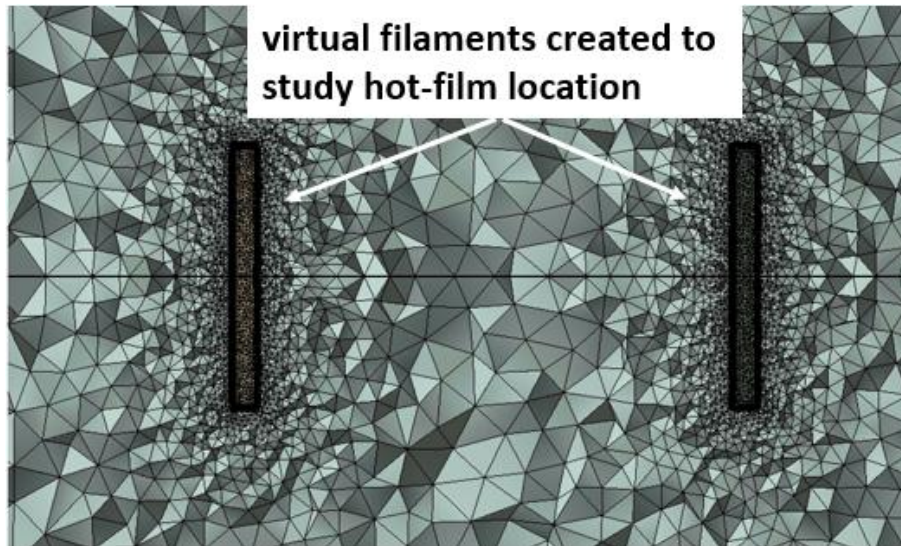
Figure 6.1 Dimension of the modified probe cap in English units.

This testbed is used to find the proper hot-film location that the flow condition at the hot-film sensing plane in the wind tunnel experiments could match the corresponding flow condition in the calibration so that error in the composition measurement could be minimized. For the computational study, a probe without any internal sensors is used since the hot-film location is unknown at this point.

In figure 6.2, fourteen virtual hot-film filaments are meshed starting from section 3 to section 5 using the same method described in section 5.3. The first two sampled locations are used to showcase the jet effect instead of an actual available hot-film location due to the length of the probe and the hot-film sensor.



(a)



(b)

Figure 6.2 Mesh of the testbed probe (a) with 14 local refinements to study the proper hot-film location (b) mesh around the sensing filaments

6.2 Quasi-one-dimensional Characteristics of the Testbed

Since the testbed probe design is more conservative than the original probe design, it is expected that this new design should still satisfy the flow requirement as described in section 3.2. Using the traditional adiabatic, inviscid, quasi-one-dimensional analysis on the testbed geometry, it is found that the internal gasdynamics is similar to the original design except the elongated length in certain sections and enlarged diameter at section 3 make the flow velocity even slower after the normal shock, thus the flush time (assuming hot-film placed at the end of section 3) is increased, shown in table 6.1.

Table 6.1 Characteristics of the testbed design.

Freestream Composition	M_∞	$P_{t,\infty}$ (kPa)	Normal Shock Mach Number	Normal Shock Position (%)	Flush Time (ms)
Pure Air	1.2	129.8	2.53	11.70	1.93
Pure Air	2.2	519.2	3.32	12.90	1.93
Pure Helium	1.2	129.8	2.78	11.03	0.68
Pure Helium	2.2	519.2	3.67	11.72	0.68

In table 6.1, it could be seen that the Mach number upstream of the normal shock is the same as in the original design. This is because the increase of the cross-sectional area along the first diverging section follows the same trend as in the original design. Due to the elongated section length, the shock is further away from the sensors as indicated by the normal shock position with respect to the first diverging section length. Due to the larger

cross-sectional area and thus smaller velocity in the second diverging section, the flush time for each boundary cases (pure air/pure helium) are increased.

For the external gasdynamics of the probe, it follows the same angularity restrictions as the original probe since the tip angle is kept the same. Figure 6.3 shows a plot of the internal Mach number along the probe compared with the internal cross-sectional area.

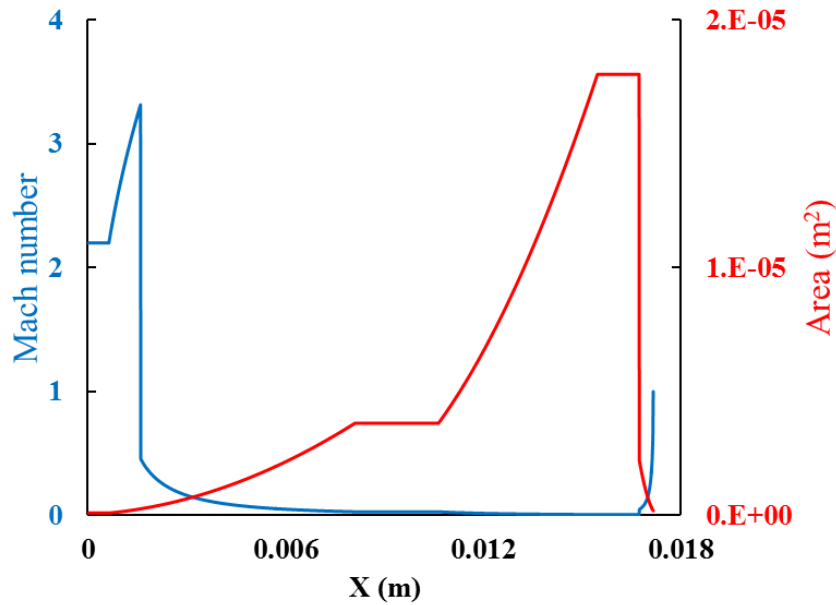


Figure 6.3 Mach number and cross-sectional area along the axial length inside the testbed.

6.3 CFD Setup of the Testbed

The CFD examination of the testbed includes a study of the testbed with the freestream conditions during the wind tunnel experiments (the freestream conditions described in chapter 4 and 5), denoted as the simulated SSWT case, and a study of the testbed in probe's calibration process, denoted as the simulated calibration case. The need of a simulated

calibration for the testbed design is to compare the flow behavior with the simulated SSWT case to determine the appropriate hot-film location while no actual testbed probe and its calibration are available.

For the simulated SSWT case, the only change is the geometry of the probe and thus the size of the computational domain. The settings remain the same as in chapter 4. Part of the domain and mesh of the testbed case is shown in figure 6.2.

During the calibration, the probe should be choked at both the inlet and the throat due to the inlet-to-throat area ratio ($A_i=0.5A_t$). The mass flow rate analysis shows that flow will become choked entering the inlet, expands supersonically until a normal shock is formed, then the velocity will decrease towards the plenum chamber before the flow accelerates again and becomes choked at the throat, shown in figure 6.4. Due to that the throat area is two times of the inlet area, the total pressure after the shock is always half of the total pressure before the shock.

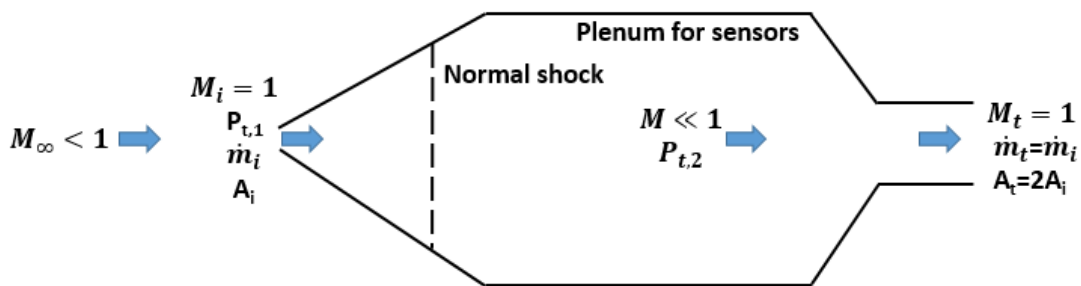
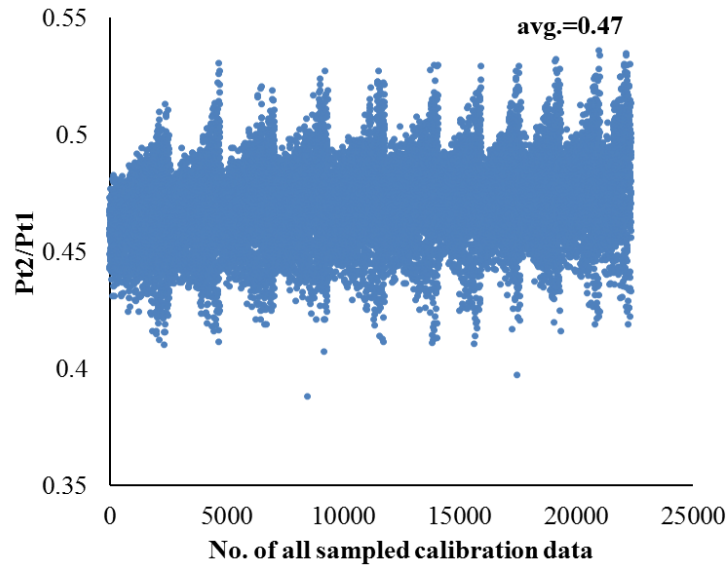


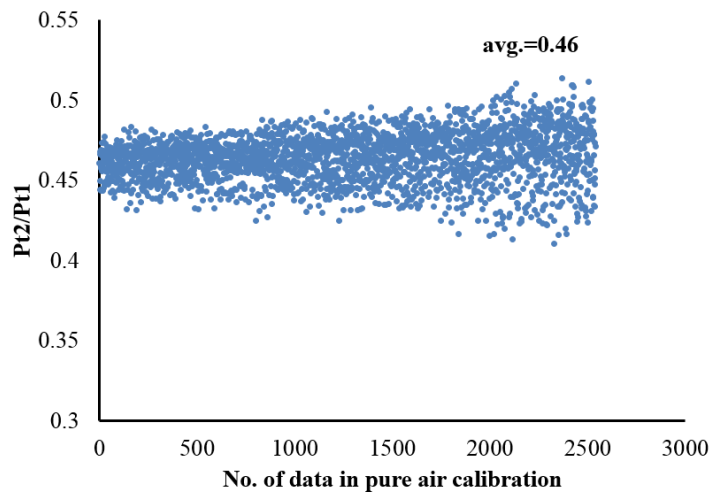
Figure 6.4 Schematic of the flow in probe calibrations.

This analysis is supported by the actual calibration data from the original probe design as total pressure measured inside the probe plenum chamber is approximately 50% of the

total pressure measured inside the calibration tank. The unfiltered data are presented in figure 6.5 with measurements of eleven compositions during the calibration. The pure air calibration is highlighted in figure 6.5(b). Pt1 is the total pressure measured inside the calibration tank, and Pt2 is the total pressure measured inside the probe's plenum chamber.



(a)



(b)

Figure 6.5 $Pt2/Pt1$ of the original two-throat probe calibration, (a) data of 11 helium concentrations (b) data of the pure air case.

In order to replicate the probe calibration in the CFD and to compare with simulations of wind tunnel test conditions, three variables need to be matched. Namely, the mass flow rate through the probe needs to be matched between the simulated SSWT case and the corresponding simulated calibration, so is the total pressure inside the probe plenum chamber between the simulated calibration case and the simulated SSWT case, and finally the relationship of the two total pressures (P_{t2}/P_{t1}) in the simulated calibration needs to be established as in the actual calibration.

Part of the domain and mesh of the simulated calibration for the testbed is shown in figure 6.6. It includes the freestream of the probe and up to the probe throat, which was shown in figure 2.3(b).

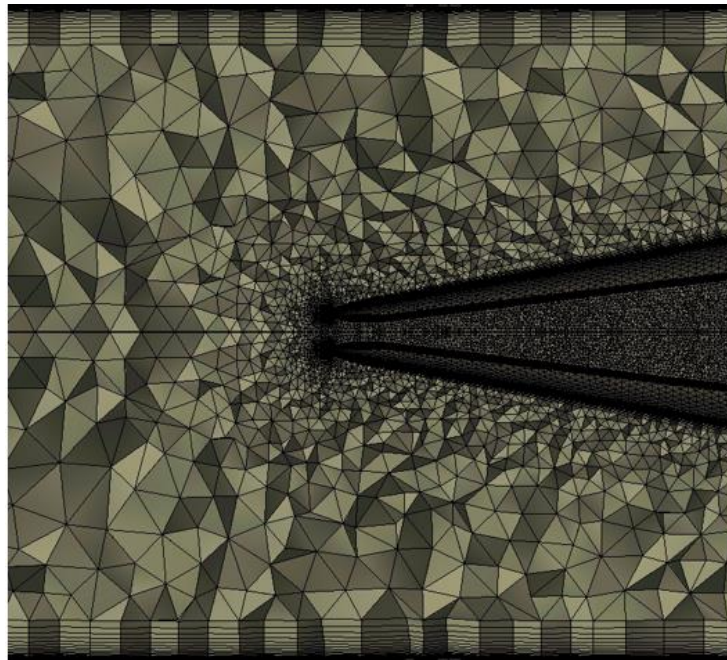


Figure 6.6 Part of the computational domain for the simulated calibration case.

All the settings are the same in the simulated calibration case as the simulated SSWT case except the boundary and initial conditions. A pressure-inlet boundary condition is used instead of the pressure-farfield boundary condition. Use the pure air case as an example, the total pressure inside the probe plenum is about 112.6 kPa from the SSWT case, so the pressure-inlet boundary conditions is set up with a total pressure of 225.2 kPa and static pressure of 225.1 kPa for initialization. The total pressure is fixed and the static pressure will be solved by the iteration process. In the simulated calibration, a standard initialization process is not sufficient to achieve the necessary convergence, indicated by the residual levels in the x-velocity and continuity equations, so that the expected pressure is patched inside the domain to help the initialization and solve the case. The boundary and initial conditions of the pure air case are shown in figure 6.7.

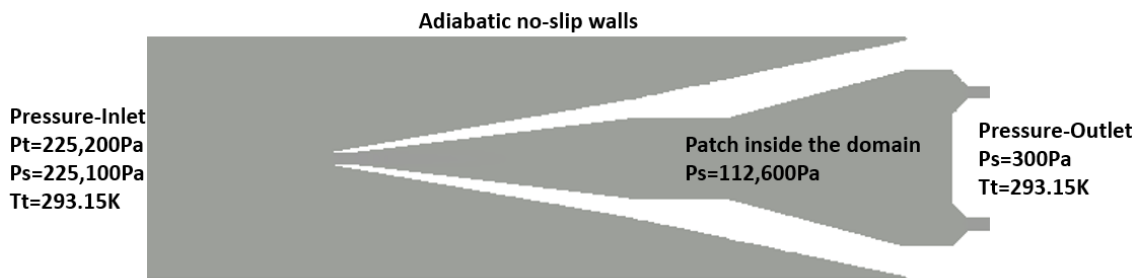


Figure 6.7 Boundary and initial conditions of the testbed in the simulated calibration.

6.4 Computational Results on the Testbed Geometry

The results of the testbed probe in the simulated SSWT case show similar flow behavior as in the original probe design in chapter 5. The Mach number contour and streamlines are shown in figure 6.8 and 6.9, respectively. It can be seen that a similar

boundary layer separation and oblique shock train formed inside the probe's first diverging section. From the Mach number contour, the jet effect at the end of the first diverging section is seen to be less severe since this section has been elongated. In addition, it can be seen that the incompressible boundary layer separation is inhibited by the smaller diverging angle in the second diverging section. These two features fulfilled the design purpose of the modified geometry in the testbed.

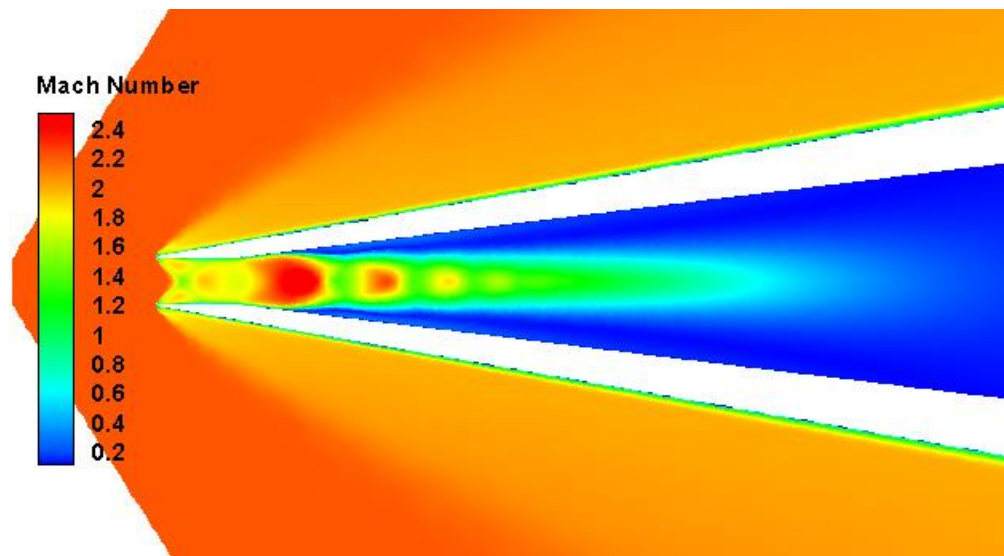
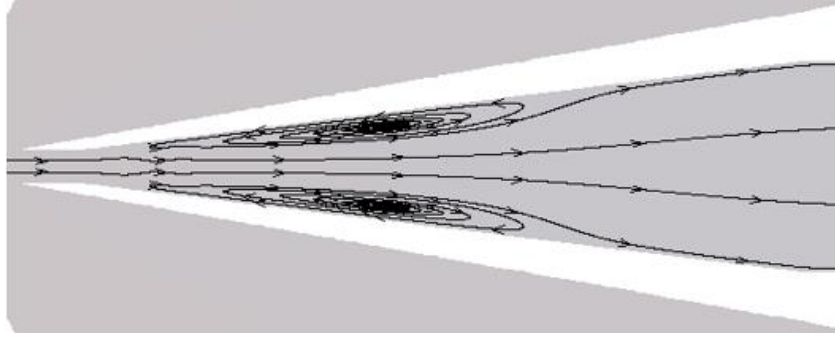
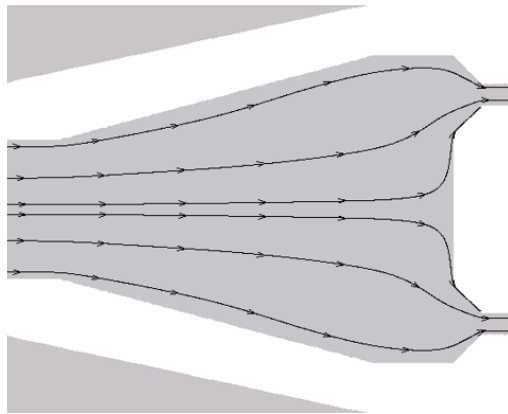


Figure 6.8 Mach number contour around the tip of the testbed in the simulated SSWT test, pure air case.



(a)



(b)

Figure 6.9 Streamlines of the testbed in the simulated SSWT test, pure air case. (a)

Frontal part of the probe, (b) aft part of the probe.

The simulated calibration of the testbed, on the other hand, shows a slightly different flow behavior compared to the simulated SSWT test. The Mach number contour and streamlines are shown in figure 6.10 and 6.11, respectively. In figure 6.10, flow is choked at the probe inlet and followed with a set of expansion and oblique shock interactions. The maximum Mach number inside the probe is approximately 1.5, lower than its corresponding simulation of wind tunnel experiments. Thus, a jet is also formed after the shock interactions but with a weaker strength.

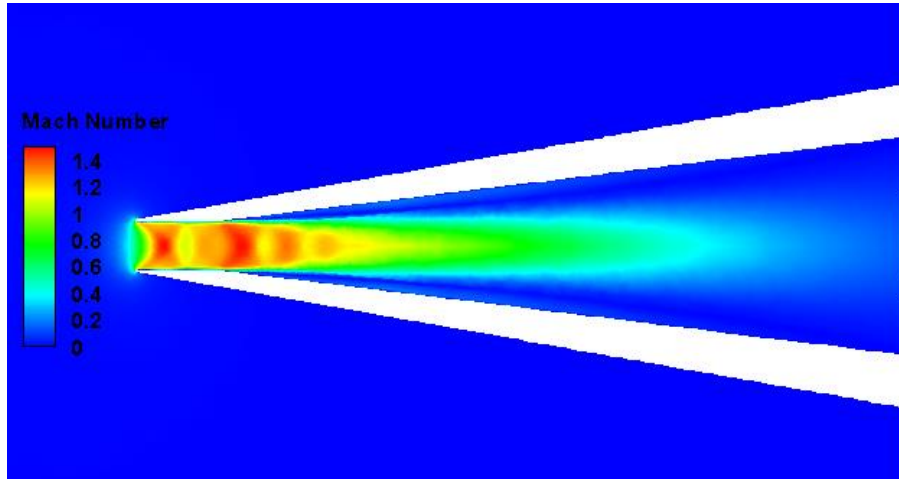
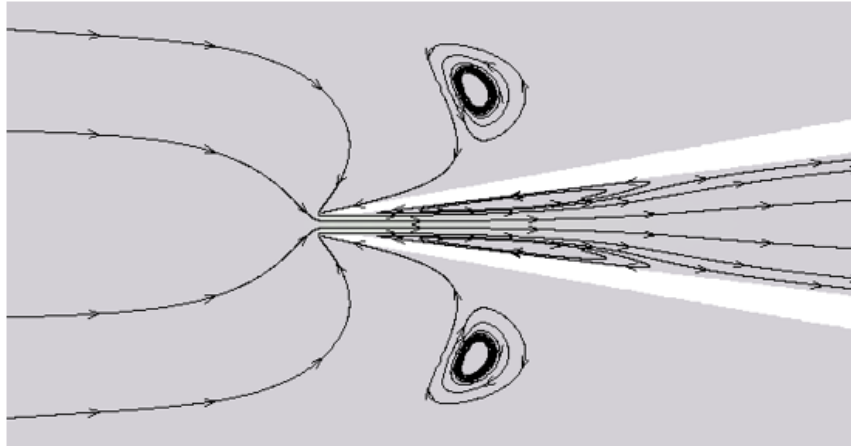
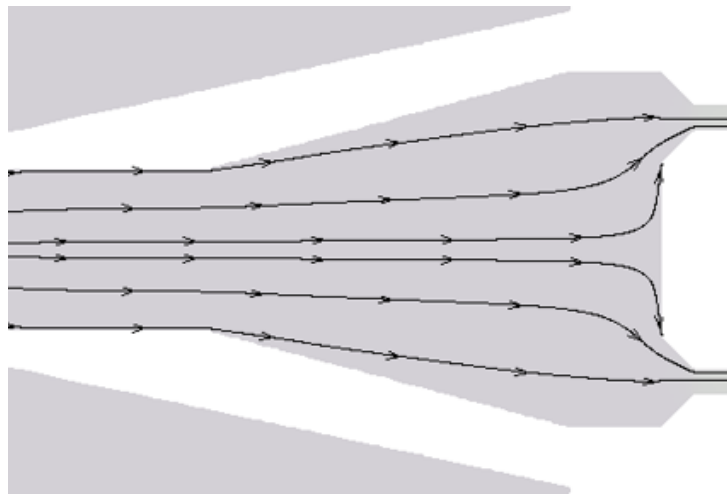


Figure 6.10 Mach number contour of the testbed in the simulated calibration test, pure air case.

In figure 6.11, it is shown that the flow in the upstream converges towards the probe before entering the probe tip. Internally after the supersonic expansion, a shock-induced boundary layer separation is formed. This creates a complex shock interactions and ends with a jet, same as what happened in the internal gasdynamics in the simulated SSWT case. The subsequent flow has a further decrease in velocity and then accelerates to be choked at the throat.



(a)



(b)

Figure 6.11 Streamlines of the testbed in the simulated calibration test, pure air case. (a)

Frontal part of the probe, (b) aft part of the probe.

With the simulated SSWT results and its corresponding simulated calibration results, the velocity profile along the hot-film's sensing plane and the mass flow rate impinging on the hot-film could be examined to give the appropriate hot-film location for minimum error in composition measurements. In figure 6.12, velocity profiles along the probe's internal

diameter are shown in 12 sampled axial stations (from stations 3 to stations 14). The x-velocity is used since the y-velocity and z-velocity account only a very small portion of the velocity vector. The length of the hot-film's sensing element is 0.254 mm, accounting less than one tenth of the internal diameter of the studied stations.

In figure 6.12, station 3 is located at the end of the first diverging section, shown in figure 6.2, and is the first studied hot-film sensing location. The velocity at station 3 of the SSWT case is shown to be higher than it is in the calibration case. This is because in the SSWT case, a higher Mach number and velocity exist when the shock-induced boundary layer separation starts compared to the calibration case. This higher velocity formed a stronger jet that according to the x-velocity profiles can influence the flow up to station 10. At station 10, the difference in the x-velocity between the calibration case and the SSWT case is small enough to be considered negligible. All subsequent downstream stations show a difference in x-velocity along the hot-film's length less than 0.5m/s. Thus, the first appropriate location of the hot-film that could minimize the error in composition measurements is said to be station 10. The pure helium case shows similar results. Considering freestream flow angularities that the probe could experience, a more conservative choice of the hot-film location to minimize the error is to extend the probe's plenum chamber, and place the hot-film at this constant cross-sectional area section.

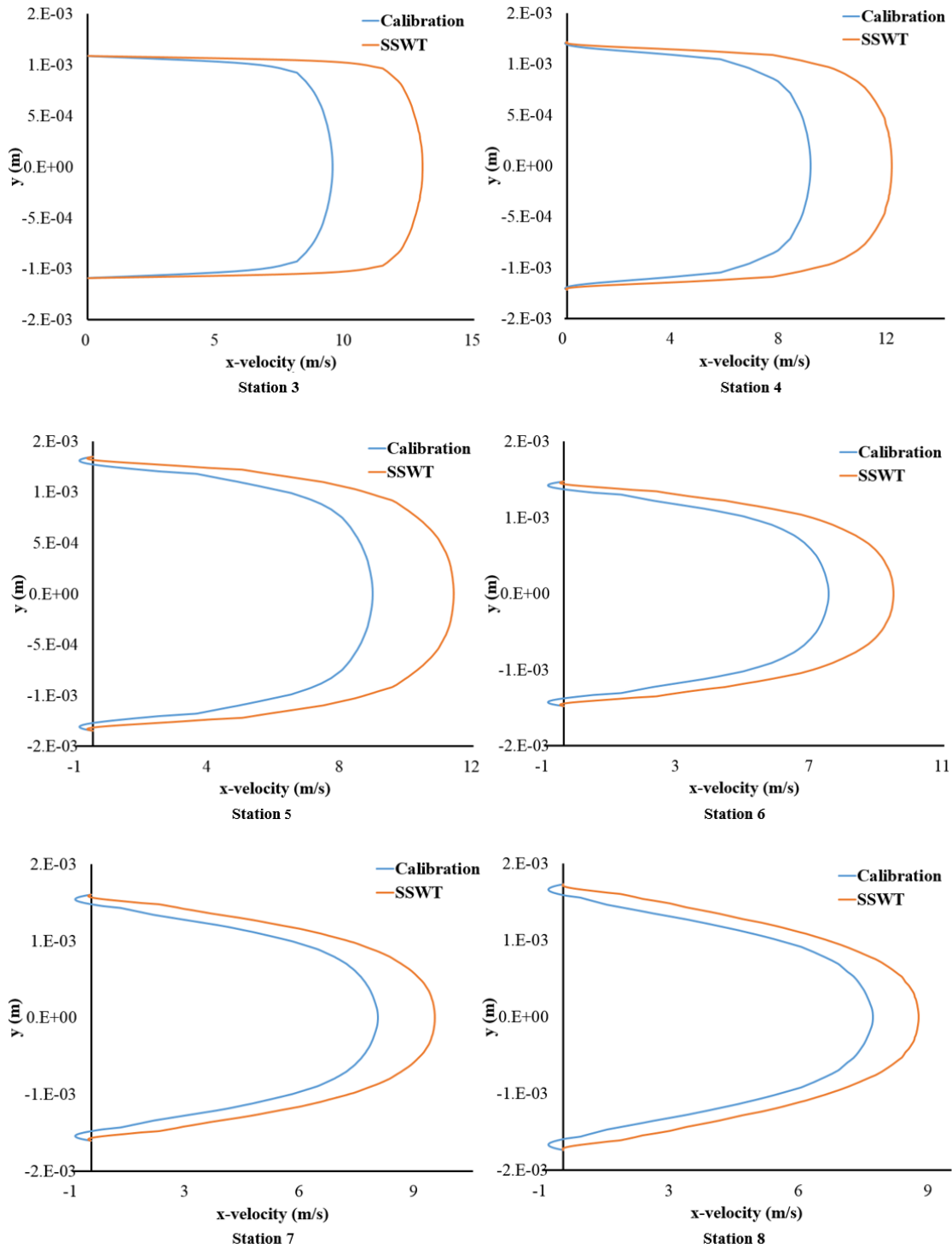


Figure 6.12 Comparison of velocity profiles along the probe's internal diameter at sampling stations between the simulated SSWT and the simulated calibration for pure air

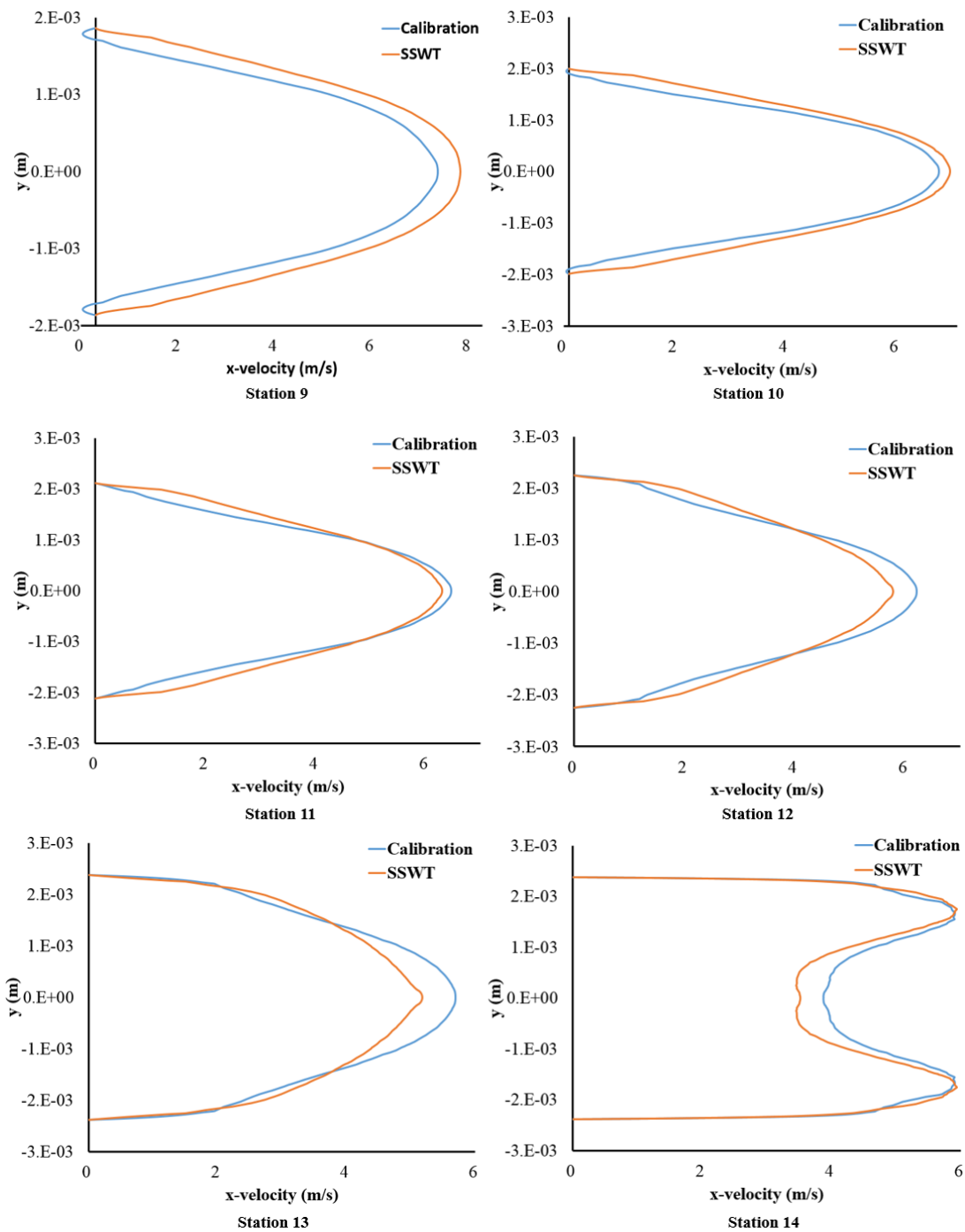


Figure 6.12(Cont.) Comparison of velocity profiles along the probe's internal diameter at sampling stations between the simulated SSWT and the simulated calibration for pure air

case.

In chapter 5, the factor F is created to evaluate the difference in the mass flow rate impinging on the hot-film between the probe operating in the SSWT and its corresponding calibration. Same procedure is performed for the simulated SSWT case and the simulated calibration case of the testbed probe. In the aforementioned velocity profile discussion, the first appropriate hot-film location with respect to the probe tip is found at station 10. The mass flow rate study for the pure air case verified this observation as the difference between the F factors in the two cases becomes less than 3% at station 10. Data at selected stations for pure air and pure helium cases are shown in table 6.2 and table 6.3, respectively.

Table 6.2 F factor at selected stations between the simulated SSWT test and calibration, pure air case.

Stations	1	3	9	10	11	14
$F \times 10^{-3}$ in SSWT	3.75	2.79	1.61	1.46	1.34	0.76
$F \times 10^{-3}$ in Calibration	2.54	2.03	1.46	1.42	1.37	0.75
% difference	+48%	+37%	+10%	+2.8%	-2.2%	+1.3%

Table 6.3 F factor at selected stations between the simulated SSWT test and calibration, pure helium case.

Stations	1	3	9	10	11	14
$F \times 10^{-3}$ in SSWT	3.38	2.61	1.85	1.77	1.68	0.89
$F \times 10^{-3}$ in Calibration	2.99	2.36	1.72	1.64	1.57	0.90
% difference	+13%	+11%	+7.6%	+7.9%	+7.0%	-1.1%

In table 6.2 and table 6.3, the largest difference in F factor among the sampled stations is at station 1 and the difference decreases as it becomes further downstream. This trend and high difference in station 1 is very consistent with the analysis of the original probe presented in section 5.4. It indicates that the hot-film should not be placed too close to the probe tip as the velocity is affected by the different strength of the jet between the wind tunnel test and the corresponding calibration. This helps decide the proper location of the hot-film as the traditional inviscid quasi-one-dimensional analysis will always predict the same velocity for the SSWT and the calibration case since station 1 no matter the upstream scenario.

In table 6.2, station 10 and stations further downstream all have less than 3% difference in the F factor for the pure air case and less than 8% for the pure helium case. In summary, the closest position of the hot-film sensor with respect to the probe tip that could avoid a large error in composition measurement is at station 10. Both cases show around 1% difference entering the plenum section so a further downstream location could be chosen

to be more conservative and minimize the error that could also be affected by a freestream flow-probe misalignment.

Chapter 7

Conclusion

Traditionally, concentration probes have been designed based on an adiabatic, inviscid, quasi-one-dimensional analysis procedure. However, this study using a detailed CFD analysis has been able to examine the internal gasdynamics of such probes with full three-dimensional viscous effects in order to better understand the probes' performance.

7.1 Summary of the CFD Findings and Recommendations

From the CFD study of the probe described in this work, it is shown that there is a significant change in the internal gasdynamics with respect to the one analyzed by the inviscid quasi-one-dimensional flow. In the three-dimensional viscous scenario a shock-induced boundary layer separation which forms an oblique shock train inside the probe is observed instead of the simple normal shock solution predicted by the inviscid quasi-one-dimensional analysis. It not only adds an internal-occurring mixing effect but also the resulting jet, caused by the boundary layer separation, severely affects the hot-film's measurement. Since the probe is working in a vortex-dominated flow, the flow-probe misalignment is proved to be another source that could add an uncertainty to the composition measurement. Thus the error in composition measurements is the major issue in designing the concentration probe.

In addition, another flow separation is observed in the second diverging section,

forming a large recirculation region. This prediction indicates the currently designed diverging angle is too large. As the pressure transducer and thermocouple are located at this region, their measurements could also be affected by this flow separation.

In chapter 6, a new design of the probe is conceived based on the CFD data in chapter 5. The more conservative design is examined by the CFD to find an appropriate hot-film location that could minimize the error in composition measurements due to viscous effects and flow-probe misalignments. Results indicate a further downstream hot-film location is preferable to minimize such error in composition measurements.

From these CFD findings, it is recommended that within the manufacturing capability the probe should have a smaller external tip angle to have more tolerance on freestream flow angularities, a smaller internal diverging angle to avoid flow separation, and most importantly, a compromise in the length of the probe for the hot-film to be sufficiently away from the shock interactions upstream and minimize the mismatch of flow conditions between the calibration and wind tunnel experiments.

7.2 Future Work

The CFD methodology described in chapter 4 provides an alternative and indispensable way to design and examine the concentration probe. While the methodology is developed for the specific probe used in this study, it could be applied to more general cases. This CFD study was used to examine the probe and associated errors in steady-state with the SST k- Ω turbulence model. However, since no direct observation of the internal

gasdynamics is available, it is difficult to say that if the current turbulence model under-predicts or over-predicts the boundary layer separation shown in chapter 5. It is suggested that different turbulence models should be utilized to form a library of possible flow behaviors. A transient simulation could also be studied to validate the phenomena that were observed. With more computational resources available, large eddy simulation or direct numerical simulation could also be used to study the concentration probe.

References

- [1] P.L. Blackshear, L. Fingerson, Rapid-Response Heat Flux Probe for High Temperature Gases, Am. Rocket Soc. J. 32, p 1709-1715, 1962.
- [2] G.L. Brown, M.R. Rebollo, A Small, Fast-Response Probe to Measure Composition of a Binary Gas Mixture, AIAA J., Vol.10, p 649-652, 1972.
- [3] J.F. Devillers, G.B. Diep, Hot-wire Measurements of Gas Mixture Concentrations in a Supersonic Flow, DISA info. 14, p 29-36, 1973.
- [4] T.A. Ninnemann, W.F. Ng, A Concentration Probe for the Study of Mixing in Supersonic Shear Flows, Experiments in Fluids. 13, p 98-104, 1992.
- [5] J.D. Wiswall, Development and Operation of an Integrated Sampling Probe and Gas Analyzer for Turbulent Mixing Studies in Complex Supersonic Flows, Master's Thesis, the University of Texas at Arlington, 2013.
- [6] O.C. Xillo, A Sampling Probe for Fluctuating Concentration Measurements in Supersonic Flow, Master's Thesis, Virginia Polytechnic Institute and State University, 1998.
- [7] L. Maddalena, Investigations of Injectors for Scramjet Engines, PhD Dissertation, Virginia Polytechnic Institute and State University, 2007.
- [8] F. Vergine, C. Ground, L. Maddalena, Experimental Study of Strut Injectors for Scramjet Combustors: Total Pressure Losses in a Selected Supersonic Streamwise Vortex Interaction Mode, AIAA 2015-3589.
- [9] J.D.Jr. Anderson, Fundamentals of Aerodynamics, 3rd ed., McGraw-Hill, New York,

2001.

[10] TSI Model 1750 Constant Temperature Anemometer User's Manual, Revision N, TSI Incorporated, February 2008.

[11] E.O. Doebelin, Measurement Systems: Applications and Design, 5th ed., McGraw-Hill, New Delhi, India, 2004.

[12] C.R. Wilke, A Viscosity Equation for Gas Mixtures, The Journal of Chemical Physics, 18 (4): 517-519, 1950.

[13] R.P. Fuller, Fuel Vortex Interactions for Enhanced Mixing in Supersonic Flow, PhD Dissertation, Virginia Polytechnic Institute and State University, 1996.

[14] D.R. Chapman, D.M. Kuehn, H.K. Larson, Investigation of Separating Flows in Supersonic and Subsonic Streams with Emphasis on the Effects of Transition, NACA Rept. 1356, 1958.

[15] V.M. Falkner, S.W. Skan, Some Approximate Solutions of the Boundary Layer Equations, Aeronautical Research Council, ARC R&M 1314, London, 1930.

[16] J.A. Schetz and R.D.W. Bowersox, Boundary Layer Analysis, 2nd Edition, AIAA Education Series, 2011, p 102-105.

Biographical Information

Wenbo Zhu was born in 1989 in Nanjing, China. In 2008, he graduated from Jinling High School in Nanjing. In the same year, he began his Bachelor's Degree in the Life Science Department at Shandong University. In 2012, he graduated from Shandong University with a Bachelor's Degree in Biotechnology. Wenbo enrolled at the University of Texas at Arlington in 2012 to pursue a graduate degree in Aerospace Engineering, being grateful for the opportunity to explore his specific field of interest at a higher academic level. He earned his Master's Degree in Aerospace Engineering from UTA in May 2016 and plans to pursue a PhD degree in the near future.

Appendix A Matlab Scripts

A.1

Inviscid, Quasi-one-dimensional Analysis Code

```
% Created by Wenbo Zhu %
% 2014/10/21 %
% final edited 2016/03/15 %
clc
clear all
close all

% geometry inputs %
N=2000;
x=linspace(0,0.4658*0.0254,N); % unit: all metric, m, from straight inlet to throat
di=0.0135*0.0254; % straight inlet
dhf=0.0520*0.0254; % hot-film section
dp=0.1875*0.0254; % main plenum
dc=0.0469*0.0254; % chamfer start diameter, diameter of one chamfer
dt=0.0135*0.0254; % diameter of one throat
thetai1=7*pi/180;
thetao1=10*pi/180;
thetai2=30*pi/180;
thetao2=22.5*pi/180;
thetac=45*pi/180;
Ai=pi*di^2/4;
Ahf=pi*dhf^2/4;
Ap=pi*dp^2/4;
% two throats %
Ac=pi*dc^2/2; % chamfer start, one throat(/4), tow throats(/2)
At=pi*dt^2/2; % one throat(/4) or two throat(/2)
Li=0.025*0.0254; % straight inlet
L1d=0.1568*0.0254; % first diverging section
Lhf=0.1*0.0254;
L2d=0.1173*0.0254; % second divergent part
Lp=0.05*0.0254; % main plenum
Lc=0.0167*0.0254; % Lc is the first chamfer
L=Li+L1d+Lhf+L2d+Lp+Lc;

% total volume of system from inlet to throat %
Vi=pi*Li*(di/2)^2;
V1d=(pi*L1d/3)*((dhf/2)^2+(di/2)^2+(di/2)*(dhf/2));
Vhf=(pi*(dhf/2)^2)*Lhf;
```

```

V2d=(pi*L2d/3)*((dp/2)^2+(dhf/2)^2+(dp/2)*(dhf/2));
Vp=(pi*(dp/2)^2)*Lp;
Vc=(pi*Lc/3)*((dt/2)^2+(dc/2)^2+(dt/2)*(dc/2))*2; %%% first chamfer, two throats or
one throat
V=Vi+V1d+Vhf+V2d+Vp+Vc;

```

```

fprintf('Geometry Inputs(metric)\n\n')
fprintf('  Ai=%d\n\n',Ai)
fprintf('  Ahf=%d\n\n',Ahf)
fprintf('  Ap=%d\n\n',Ap)
fprintf('  Ac=%d\n\n',Ac)
fprintf('  At=%d\n\n',At)
fprintf('  Li=%d\n\n',Li)
fprintf('  L1d=%d\n\n',L1d)
fprintf('  Lhf=%d\n\n',Lhf)
fprintf('  L2d=%d\n\n',L2d)
fprintf('  Lp=%d\n\n',Lp)
fprintf('  Lc=%d\n\n',Lc)
fprintf('  L=%d\n\n',L)
fprintf('  volume of probe from inlet to throat V(m^3)=%d\n\n',V)
Ait=Ai/At;
fprintf('  Ai/At=%d\n\n',Ait)

```

```

% aerodynamic inputs %
fprintf('Aerodynamic Inputs\n\n')
Mi=2.2; % around 1.2-2.2
fprintf('  Mi=%d\n\n',Mi)
g=1.4; % 1.4 for pure air; 1.6667 for helium
fprintf('  gamma=%d\n\n',g)
Tt=293.15;
fprintf('  Tt=%d\n\n',Tt)
R=287; % 287 for pure air; 2077 for helium
fprintf('  R=%d\n\n',R)

```

```

% probe geometry plot %
for i=1:N
    if x(i)<=Li % inlet
        r(i)=di/2;
        A(i)=pi*r(i)^2;
    elseif x(i)>Li && x(i)<=Li+L1d % 1st diverging section
        r(i)=di/2+(x(i)-Li)*tan(theta1);
    end
end

```

```

    A(i)=pi*r(i)^2;
elseif x(i)>Li+L1d && x(i)<=Li+L1d+Lhf % hot-film section
    r(i)=dhf/2;
    A(i)=Ahf;
elseif x(i)>Li+L1d+Lhf && x(i)<=Li+L1d+Lhf+L2d % second divergent duct
    r(i)=dhf/2+(x(i)-(Li+L1d+Lhf))*tan(thetai2);
    A(i)=pi*r(i)^2;
elseif x(i)>Li+L1d+Lhf+L2d && x(i)<=Li+L1d+Lhf+L2d+Lp % plenum
    r(i)=dp/2;
    A(i)=Ap;
else % first chamfer
    r(i)=(dc/2-(x(i)-(Li+L1d+Lhf+L2d+Lp))*tan(thetac));
    A(i)=2*pi*r(i)^2;    %% two throats or one throats
end
end
figure (1)
plot(x,r)
title('geometry of Probe')
xlabel('x(m)')
ylabel('r(m)')
axis([0,0.4658*0.0254,0,0.1*0.0254])

figure (2)
plot(x,A)
title('Area of Probe along x')
xlabel('x(m)')
ylabel('A(m^2)')
axis([0,0.4658*0.0254,0,0.03*0.0254^2])

% the position of shock %
fprintf('Outputs\n\n')
Aistar=((((g+1)/2)^(-(g+1)/(2*g-2)))*((1+(g-1)*Mi^2/2)^((g+1)/(2*g-2)))/Mi; % Ai/Astar
Astar=Ai/Aistar;
fprintf('  Astar=%d\n\n',Astar)
Pt21=Ait/Aistar; % Pt2/Pt1
fprintf('  Pt2/Pt1=%d\n\n',Pt21)
f=@(Ms1) ((g+1)*Ms1^2/((g-1)*Ms1^2+2))^(g/(g-1))*((g+1)/(2*g*Ms1^2-(g-1)))^(1/(g-1));
X=fzero(@(Ms1) f(Ms1)-Pt21,3);
Ms1=X;
fprintf('  Ms1=%d\n\n',Ms1)

```

```

a1=((1+(g-1)*Ms1^2/2)/((g+1)/2))^(g+1)/(2*(g-1));
b1=((1+(g-1)*Mi^2/2)/((g+1)/2))^(-(g+1)/(2*(g-1)));
Asi=(Mi/Ms1)*a1*b1; % As/Ai
fprintf('  As/Ai=%d\n\n',Asi)

As=Ai*Asi;
fprintf('  As=%d\n\n',As)

s=(sqrt(As/pi)-sqrt(Ai/pi))/tan(thetai1);
fprintf('  shock position from 1st diverging section x=%d\n\n',s)

s2=s+Li;
fprintf('  shock position from tip x=%d\n\n',s2)

% shock properties before and after %
Ms2=sqrt(((g-1)*Ms1^2+2)/(2*g*Ms1^2-(g-1)));
fprintf('  Ms2=%d\n\n',Ms2)
P21=(2*g*Ms1^2-(g-1))/(g+1); % P2/P1
T21=(2*g*Ms1^2-(g-1))*((g-1)*Ms1^2+2)/((g+1)^2*Ms1^2); % T2/T1
Asstar=((((g+1)/2)^(-(g+1)/(2*g-2)))*((1+(g-1)*Ms2^2/2)^(g+1)/(2*g-2)))/Ms2;
Astar2=As/Asstar; % Astar after the shock
fprintf('  Astar2=%d\n\n',Astar2)

% Mach number, pressure, temperature, velocity along probe %
for i=1:N
    if x(i)<Li
        Ma(i) = Mi;
        PPt(i)=(1+(g-1)*Ma(i)^2/2)^(-g/(g-1)); % P/Pt1
        TTt(i)=(1+(g-1)*Ma(i)^2/2)^-1;
        T(i)=Tt*TTt(i);
        a(i)=sqrt(g*R*T(i));
        v(i)=a(i)*Ma(i);
    elseif x(i)>=Li && x(i)<s2 % before shock
        f = @(M) ( (((g+1)/2)^(-(g+1)/(2*g-2)))*((1+(g-1)*M^2/2)^(g+1)/(2*g-2)))/M) -
        A(i)/Astar );
        Ma(i) = fzero(f,Ms1);
        PPt(i)=(1+(g-1)*Ma(i)^2/2)^(-g/(g-1)); % P/Pt1
        TTt(i)=(1+(g-1)*Ma(i)^2/2)^-1;
        T(i)=Tt*TTt(i);

```

```

a(i)=sqrt(g*R*T(i));
v(i)=a(i)*Ma(i);
elseif x(i)==s2 % at shock
Ma(i)=Ms2;
PPt(i)=(1+(g-1)*Ma(i)^2/2)^(-g/(g-1));
TTt(i)=(1+(g-1)*Ma(i)^2/2)^-1;
T(i)=Tt*TTt(i);
a(i)=sqrt(g*R*T(i));
v(i)=a(i)*Ma(i);
elseif x(i)>s2 && x(i)<=Li+L1d+Lhf % inlet after shock to hot film plane
f = @(M) ( (((g+1)/2)^(-(g+1)/(2*g-2)))*((1+(g-1)*M^2/2)^((g+1)/(2*g-2)))/M) -
A(i)/Astar2 );
Ma(i) = fzero(f,0.35);
PPt(i)=(1+(g-1)*Ma(i)^2/2)^(-g/(g-1)); % P/Pt2
TTt(i)=(1+(g-1)*Ma(i)^2/2)^-1;
T(i)=Tt*TTt(i);
a(i)=sqrt(g*R*T(i));
v(i)=a(i)*Ma(i);
elseif x(i)>Li+L1d+Lhf && x(i)<=Li+L1d+Lhf+L2d % second diverget part
f = @(M) ( (((g+1)/2)^(-(g+1)/(2*g-2)))*((1+(g-1)*M^2/2)^((g+1)/(2*g-2)))/M) -
A(i)/Astar2 );
Ma(i) = fzero(f,0.05);
PPt(i)=(1+(g-1)*Ma(i)^2/2)^(-g/(g-1)); % P/Pt2
TTt(i)=(1+(g-1)*Ma(i)^2/2)^-1;
T(i)=Tt*TTt(i);
a(i)=sqrt(g*R*T(i));
v(i)=a(i)*Ma(i);
elseif x(i)>Li+L1d+Lhf+L2d && x(i)<=Li+L1d+Lhf+L2d+Lp % plenum
f = @(M) ( (((g+1)/2)^(-(g+1)/(2*g-2)))*((1+(g-1)*M^2/2)^((g+1)/(2*g-2)))/M) -
A(i)/Astar2 );
Ma(i) = fzero(f,0.01);
PPt(i)=(1+(g-1)*Ma(i)^2/2)^(-g/(g-1)); % P/Pt2
TTt(i)=(1+(g-1)*Ma(i)^2/2)^-1;
T(i)=Tt*TTt(i);
a(i)=sqrt(g*R*T(i));
v(i)=a(i)*Ma(i);
elseif x(i)>Li+L1d+Lhf+L2d+Lp && x(i)<Li+L1d+Lhf+L2d+Lp+Lc
f = @(M) ( (((g+1)/2)^(-(g+1)/(2*g-2)))*((1+(g-1)*M^2/2)^((g+1)/(2*g-2)))/M) -
A(i)/Astar2 );
Ma(i) = fzero(f,0.4);
PPt(i)=(1+(g-1)*Ma(i)^2/2)^(-g/(g-1)); % P/Pt2

```

```

TTt(i)=(1+(g-1)*Ma(i)^2/2)^-1;
T(i)=Tt*TTt(i);
a(i)=sqrt(g*R*T(i));
v(i)=a(i)*Ma(i);
else
Ma(i) = 1;
PPt(i)=(1+(g-1)*Ma(i)^2/2)^(-g/(g-1)); % P/Pt2
TTt(i)=(1+(g-1)*Ma(i)^2/2)^-1;
T(i)=Tt*TTt(i);
a(i)=sqrt(g*R*T(i));
v(i)=a(i)*Ma(i);
end
end

```

```

% plots %
figure (3)
plot(x, Ma)
title('Mach inside Probe along x')
xlabel ('x(m)');
ylabel ('Mach');
axis([0,0.4658*0.0254,0,3])

```

```

figure (4)
plot(x, PPt)
title('Ps/Pt inside Probe along x')
xlabel ('x(m)');
ylabel ('Ps/Pt');
axis([0,0.4658*0.0254,0,1])

```

```

figure (5)
plot(x, TTt)
title('Ts/Tt inside Probe along x')
xlabel ('x(m)');
ylabel ('Ts/Tt');
axis([0,0.4658*0.0254,0,1])

```

```

figure (6)
plot(x, T)
title('T inside Probe along x')
xlabel ('x(m)');
ylabel ('T(K)');

```

```
axis([0,0.4658*0.0254,0,300])
```

```
figure (7)
```

```
plot(x,a)
```

```
title('speed of sound inside Probe along x')
```

```
xlabel ('x(m)');
```

```
ylabel ('a(m/s)');
```

```
axis([0,0.4658*0.0254,0,1000])
```

```
figure (8)
```

```
plot(x,v)
```

```
title('velocity inside Probe along x')
```

```
xlabel ('x(m)');
```

```
ylabel ('v(m/s)');
```

```
axis([0,0.4658*0.0254,0,800])
```

```
figure (9)
```

```
[ax,p1,p2] = plotyy(x,Ma,x,A,'plot');
```

```
%title('Mach & Area along the probe')
```

```
ylabel(ax(1),'Mach number','FontSize',14,'FontWeight','bold')
```

```
ylabel(ax(2),'Area(m^2)','FontSize',14,'FontWeight','bold')
```

```
xlabel(ax(2),'x(m)','FontSize',14,'FontWeight','bold')
```

```
set(ax(1),'FontSize',14,'FontWeight','bold')
```

```
set(ax(2),'FontSize',14,'FontWeight','bold')
```

```
%% probe fill time %%
```

```
Lo=Li+L1d+Lhf+L2d+Lp+Lc;
```

```
fillt=0;
```

```
for i=1:2000
```

```
    dx=Lo/2000;
```

```
    dt=dx/v(i);
```

```
    fillt=fillt+dt;
```

```
end
```

```
fprintf('  fill time of the probe t(s)=%d\n\n',fillt)
```

```
% calculate flush time from hot-film to throat
```

```
N2=2000;
```

```
xx=linspace(0,0.2567*0.0254,N2);
```

```
for j=1:N2
```

```
    if xx(j)<=0.19*0.0254-L2d % start from hot-film
```

```
        rr(j)=dhf/2;
```

```

        AA(j)=pi*rr(j)^2;
elseif xx(j)>0.0727*0.0254 && xx(j)<=0.19*0.0254 % 2nd diverging section
    rr(j)=dhf/2+(xx(j)-0.0727*0.0254)*tan(thetai2);
    AA(j)=pi*rr(j)^2;
elseif xx(j)>0.19*0.0254 && xx(j)<=0.24*0.0254 % main plenum section
    rr(j)=dp/2;
    AA(j)=Ap;
else % first chamfer
    rr(j)=(dc/2-(xx(j)-(0.24*0.0254))*tan(thetac));
    AA(j)=2*pi*rr(j)^2;    %% two throats or one throats
end
end
figure (11)
plot(xx,rr)
title('geometry of Probe from hot-film to throat')
xlabel('x(m)')
ylabel('r(m)')
axis([0,0.2567*0.0254,0,0.1*0.0254])

figure (12)
plot(xx,AA)
title('Area of Probe along x')
xlabel('x(m)')
ylabel('A(m^2)')
axis([0,0.2567*0.0254,0,0.03*0.0254^2])

for j=1:N2
    if xx(j)<=0.0727*0.0254 % hot film plane
        f = @(M) ( (((g+1)/2)^(-(g+1)/(2*g-2)))*((1+(g-1)*M^2/2)^((g+1)/(2*g-2)))/M) -
AA(j)/Astar2 );
        Ma2(j) = fzero(f,0.1);
        TTt2(j)=(1+(g-1)*Ma2(j)^2/2)^-1;
        T2(j)=Tt*TTt2(j);
        a2(j)=sqrt(g*R*T2(j));
        vv(j)=a2(j)*Ma2(j);
    elseif xx(j)>0.0727*0.0254 && xx(j)<=0.0727*0.0254+L2d % second diverget part
        f = @(M) ( (((g+1)/2)^(-(g+1)/(2*g-2)))*((1+(g-1)*M^2/2)^((g+1)/(2*g-2)))/M) -
AA(j)/Astar2 );
        Ma2(j) = fzero(f,0.05);
        TTt2(j)=(1+(g-1)*Ma2(j)^2/2)^-1;
        T2(j)=Tt*TTt2(j);
    end
end

```

```

a2(j)=sqrt(g*R*T2(j));
vv(j)=a2(j)*Ma2(j);
elseif xx(j)>0.0727*0.0254+L2d && xx(j)<=0.0727*0.0254+L2d+Lp % plenum
f = @(M) ( (((g+1)/2)^(-(g+1)/(2*g-2)))*((1+(g-1)*M^2/2)^((g+1)/(2*g-2)))/M) -
AA(j)/Astar2 );
Ma2(j) = fzero(f,0.01);
TTt2(j)=(1+(g-1)*Ma2(j)^2/2)^-1;
T2(j)=Tt*TTt2(j);
a2(j)=sqrt(g*R*T2(j));
vv(j)=a2(j)*Ma2(j);
elseif xx(j)>0.0727*0.0254+L2d+Lp && xx(j)<0.0727*0.0254+L2d+Lp+Lc-(1e-
5) % chamfer
f = @(M) ( (((g+1)/2)^(-(g+1)/(2*g-2)))*((1+(g-1)*M^2/2)^((g+1)/(2*g-2)))/M) -
AA(j)/Astar2 );
Ma2(j) = fzero(f,0.4);%0.5 for air, 0.4 for helium
TTt2(j)=(1+(g-1)*Ma2(j)^2/2)^-1;
T2(j)=Tt*TTt2(j);
a2(j)=sqrt(g*R*T2(j));
vv(j)=a2(j)*Ma2(j);
else % throat
Ma2(j) = 1;
TTt2(j)=(1+(g-1)*Ma2(j)^2/2)^-1;
T2(j)=Tt*TTt2(j);
a2(j)=sqrt(g*R*T2(j));
vv(j)=a2(j)*Ma2(j);
end
end

```

```

figure (13)
plot(xx,Ma2)
title('Mach inside Probe along x')
xlabel ('x(m)');
ylabel ('Mach');
axis([0,0.2567*0.0254,0,1])

```

```

figure (14)
plot(xx,vv)
title('velocity inside Probe along x')
xlabel ('x(m)');
ylabel ('v(m/s)');
axis([0,0.2567*0.0254,0,350])

```

```
%% probe flush time %%  
LL=0.0727*0.0254+L2d+Lp+Lc;  
flusht=0;  
for i=1:2000  
    dxx=LL/2000;  
    dtt=dxx/vv(i);  
    flusht=flusht+dtt;  
end  
fprintf(' flush time of the probe t(s)=%d\n\n',flusht)
```

A.2 Probe Calibration Code

```
clear all
close all
clc
%% Probe Calibration Code
% Load data file & define nominal calibration points
% read raw_data from the file, time Ptank Pprobe T V X_He
% Pressure is in psi, other parater are in SI units
raw_data=xlsread('20160210.xlsx');

P_array=(35:-5:15); % nominal pressures in data file % 60->10
X_array=(0:0.1:1); % concentration in data file % 0->1
P_tol=0.35; % pressure tolerance 0.5 psia
delP=P_array(1)-P_array(2); % pressure step, 10 psia

% correction of data
raw_data(:,2)=0.9955*raw_data(:,2)+0.1923; % correct Ptank
raw_data(:,4)=raw_data(:,4); % correct T

% Filter out data outside pressure tolerances
good_data=zeros(length(raw_data),4); % pre-allocate the array, size only refer to rows,
good_data has the same size of Raw_data but all blocks are 0 now
i3=0;
for i1=1:1:length(raw_data)
    for i2=1:1:length(P_array)
        if abs(raw_data(i1,3)-P_array(i2))<=P_tol
            i3=i3+1;
            good_data(i3,1)=raw_data(i1,3);
            good_data(i3,2)=raw_data(i1,4);
            good_data(i3,3)=raw_data(i1,5);
            good_data(i3,4)=raw_data(i1,6);
        end
    end
end
good_data(all(good_data==0,2),:)=[];
xlswrite('good data in calibration.xlsx',good_data)
% average data and reorder
avg_data=zeros(size(good_data));
i15=0;
```

```

x22=0;
for i11=1:1:length(X_array)
    for i12=1:1:length(P_array)
        x12=0;
        i14=0;
        x22=0;
        x32=0;
        for i13=1:1:length(good_data)
            if abs(good_data(i13,4)-X_array(i11))<=0.01
                if abs(good_data(i13,1)-P_array(i12))<=P_tol
                    x11=good_data(i13,1);           % average P, T, V
                    respectively
                    x12=x12+x11;
                    i14=i14+1;
                    x21=good_data(i13,2);
                    x22=x22+x21;
                    x31=good_data(i13,3);
                    x32=x32+x31;
                end
            end
            x13=x12/i14;
            x23=x22/i14;
            x33=x32/i14;
            if x12~=0
                i15=i15+1;
                avg_data(i15,2)=x13;           % P
                avg_data(i15,3)=x23;           % T
                % avg_data(i15,2)=good_data(1,2); % T
                avg_data(i15,1)=X_array(i11); % X_He
                avg_data(i15,4)=x33;           % V
            end
        end
    end
end
avg_data(all(avg_data==0,2),:)=[];

% sort data so coloums are X_He increase, Pt increase, Tt, V
sorted_data=sortrows(avg_data,[1 2]); % ascending order in the P
xlswrite('calibration f factor.xlsx',sorted_data)

X_He=sorted_data(:,1);

```

```

P=sorted_data(:,2);
T_avg=sum(sorted_data(:,3))/length(sorted_data);
T_array=zeros(length(sorted_data),1);
T_array(:,1)=T_avg;
T=T_array;
V=sorted_data(:,4);
X_air=1-X_He;

% Probe Variables
R_series=20+0.2+0.55; % Series bridge resistance, 20+cable+lead res
R_film=7.05; % Hot film "hot" resistance
T_film=273.15+247.24; % Constant hot-film temperature in Kelvin
l_film=250e-6; % hot film sensing length in meters
d_film=25.4e-6; % diameter of the hot-film in meters

d_throat=0.0135*0.0254; % diameter of the throats in meters
d_HF=0.052*0.0254; % hot-film plane diameter in meters
A_star=2*pi*(d_throat/2)^2; %% throat area in m^2 for two throats, TWO THROAT
HERE %%
A_HF=pi*(d_HF/2)^2; % HF area in m^2

R_Uni=8314.4; % Universal gas constant in J/kg-K
M_air=28.97; % molecular weight of air
M_He=4.0026; % molecular weight of helium

% Evaluate thermodynamic properties
Cp_air=1004.5;
Cp_He=5193.0;

k_air=1.61344e-4+8.89970e-5*T+3.85599e-8*T.^2-2.39332e-10*T.^3+3.48891e-
13*T.^4-1.84858e-16*T.^5;
k_He=4.33185e-2+1.23854e-4*T+2.77149e-6*T.^2-1.11774e-8*T.^3+1.81601e-
11*T.^4-1.03892e-14*T.^5;

mu_air=-1.31554e-6+9.53265e-8*T-1.50660e-10*T.^2+2.41737e-13*T.^3-2.58576e-
16*T.^4+1.26849e-19*T.^5;
mu_He=-4.56080e-6+2.05152e-7*T-8.89707e-10*T.^2+2.41714e-12*T.^3-3.2072e-
15*T.^4+1.6306e-18*T.^5;

% Binary gas mixture calculations
M_mix=X_air*M_air+X_He*M_He;

```

```

R_mix=R_Uni./M_mix;
Cp_mix=X_air.*Cp_air.*(M_air./M_mix)+X_He.*Cp_He.*(M_He./M_mix);
gamma=Cp_mix./(Cp_mix-R_mix);
C_mix=sqrt(gamma./R_mix).*(2./(gamma+1)).^((gamma+1)/(2*(gamma-1)));

% mu and k of the mixture
% phi_air/He
Phi_mu_air_He=(1+(mu_air./mu_He).^0.5.*(M_He./M_air).^0.25).^2./(2*sqrt(2).*(1+M_
_air./M_He).^0.5);
% phi_He/air
Phi_mu_He_air=(1+(mu_He./mu_air).^0.5.*(M_air./M_He).^0.25).^2./(2*sqrt(2).*(1+M_
_He./M_air).^0.5);
% mu1
mu_mix_1=mu_air./(1+X_He./X_air.*Phi_mu_air_He);
% mu2
mu_mix_2=mu_He./(1+X_air./X_He.*Phi_mu_He_air);
% mu_mix
mu_mix=mu_mix_1+mu_mix_2;
% k
f1=k_air.*X_air+k_He.*X_He;
f2=k_air.*k_He;
f3=X_air.*sqrt(k_He)+X_He.*sqrt(k_air);
k_mix=0.5*(f1+f2./(f3.^2));

% intermideate variables
N1=(R_series+R_film)^2*pi*l_film/R_film;
N2=d_film*A_star/A_HF;
N3=k_mix.*(T_film-T);
N4=6894.76*P.*C_mix./(mu_mix.*sqrt(T));
Re=N2.*N4;
Nu=V.^2./(N1.*N3);
lnRe=log(Re);
lnNu=log(Nu);

% add calculated Re, Nu into data
new_data=zeros(length(avg_data),8);
for i4=1:1:length(avg_data)
    new_data(i4,:)= [X_He(i4),P(i4),T(i4),V(i4),Re(i4),Nu(i4),lnRe(i4),lnNu(i4)];
end

% find a&b for each concentration using least square fit, check here

```

```

ab_data=zeros(length(X_array),3);
for i5=1:1:length(X_array)                                % X_He=0,0.1,0.2...
    i7=0;
    x3=0;
    x4=0;
    y3=0;
    y4=0;
    xx=0;
    xy=0;
    for i6=1:1:length(new_data)
        if abs(new_data(i6,1)-X_array(i5))<=0.01
            x1(i6)=new_data(i6,7);% lnRe
            y1(i6)=new_data(i6,8);% lnNu
            i7=i7+1;
            x4=x4+x1(i6);          % sum of lnRe
            y4=y4+y1(i6);          % sum of lnNu
            xx=x1(i6)*x1(i6)+xx;
            xy=x1(i6)*y1(i6)+xy;
        end
    end
    x5=i7*xx-x4*x4; % average delta lnRe
    y5=i7*xy-x4*y4; % average delta lnNu
    b=y5/x5;
    a=exp((y4-b*x4)/i7);
    ab_data(i5,1)=X_array(i5);
    ab_data(i5,2)=a;
    ab_data(i5,3)=b;
end

% find c&d (same idea as a&b but for P-V diagram) for each concentration using least
square fit
cd_data=zeros(length(X_array),3);
for i105=1:1:length(X_array)                             % X_He=0,0.1,0.2...
    i107=0;
    x103=0;
    x104=0;
    y103=0;
    y104=0;
    xx10=0;
    xy10=0;
    for i106=1:1:length(new_data)

```

```

        if abs(new_data(i106,1)-X_array(i105))<=0.01
            x101(i106)=log(new_data(i106,2));
            y101(i106)=log(new_data(i106,4));
            i107=i107+1;
            x104=x104+x101(i106);
            y104=y104+y101(i106);
            xx10=x101(i106)*x101(i106)+xx10;
            xy10=x101(i106)*y101(i106)+xy10;
        end
    end
    x105=i107*xx10-x104*x104;
    y105=i107*xy10-x104*y104;
    d=y105/x105;
    c=exp((y104-d*x104)/i107);
    cd_data(i105,1)=X_array(i105);
    cd_data(i105,2)=c;
    cd_data(i105,3)=d;
end

% plot V-P diagram, least square curve, also shown scattered data points
Color=['b';'g';'r';'c';'m';'y';'k';'b';'g';'r';'c'];
figure(1);
plot_data=zeros(length(P_array),2);
for i24=1:1:length(X_array)
    P_plot=linspace(10,45,1000);
    plot(P_plot,cd_data(i24,2)*P_plot.^cd_data(i24,3),strcat('-',Color(i24)), 'LineWidth',2)
    hold on
end
for i21=1:1:length(X_array)
    i23=0;
    for i22=1:1:length(new_data)
        if abs(new_data(i22,1)-X_array(i21))<=0.01
            i23=i23+1;
            plot_data(i23,1)=new_data(i22,2);
            plot_data(i23,2)=new_data(i22,4);
        end
    end
end
plot_data(all(plot_data==0,2),:)=[];
x=plot_data(:,1);
y=plot_data(:,2);
scatter(x,y,'filled');

```

```
end
axis([0,40,1.5,4.5]);
xlabel('Pressure (psia)','FontSize',12,'FontWeight','bold');
ylabel('CTA Voltage (V)','FontSize',12,'FontWeight','bold');
%title('P-V diagram');
legend('X_H_e=0.0','X_H_e=0.1','X_H_e=0.2','X_H_e=0.3','X_H_e=0.4','X_H_e=0.5','X_H_e=0.6','X_H_e=0.7','X_H_e=0.8','X_H_e=0.9','X_H_e=1.0','Location','EastOutside');
```